1
2
Remotely sensing river greenhouse gas exchange velocity using the SWOT satellite

3
4
Craig B Brinkerhoff[1,*], Colin J Gleason[1], Christopher J Zappa[2], Peter A Raymond[3], and Merritt H Harlan[1]

5   [1] Department of Civil & Environmental Engineering, University of Massachusetts, Amherst, MA
6   [2] Lamont-Doherty Earth Observatory, Columbia University, Palisades, NY
7   [3] School of the Environment, Yale University, New Haven, CT

8   [*] Correspondence: Craig B Brinkerhoff <cbrinkerhoff@umass.edu>

9 **Key Points**

10   •   The BIKER algorithm predicts gas exchange velocity and CO_2 fluxes solely from
11   simulated SWOT data without calibration
12   •   BIKER is robust to SWOT measurement errors
13   •   BIKER will allow for novel study of gas exchange spatiotemporal dynamics after SWOT's
14   launch

15 **Keywords**

16   gas exchange, fluvial geomorphology, remote sensing, open-channel flow, SWOT,

17 biogeochemistry

18

19 **Abstract**

20   Extensive research over the past two decades has shown that the global river network emits

21 significant amounts of greenhouse gas. Despite much progress, there is still large uncertainty in

22 the temporal dynamics of gas exchange and thus carbon emissions to the atmosphere. Much of this

23 uncertainty stems from uncertainty in gas exchange velocity k_{600} (the rate of this diffusive

24 transport). We propose that the NASA/CNES/USKA/CSA SWOT satellite can provide new

25 insights to fluvial gas exchange modeling upon launch in 2022. Here, we present work inferring

26 k_{600} from synthetic future SWOT observations without in situ calibration. We exploit the unique

27 geomorphology of SWOT-observable rivers to develop a physical model of gas exchange that is

28 remotely sensible and explains 70% of variation across 166 field measurement of k_{600}. We then

29 couple this model with established inversion techniques to develop BIKER, the 'Bayesian

30 Inference of the k_{600} Exchange Rate' algorithm. We validate BIKER on 47 SWOT-simulated

31 rivers, yielding an algorithm that predicts the k_{600} timeseries solely from SWOT observations with

32 a by-river median Kling-Gupta Efficiency of 0.37. Similar to remote sensing algorithms for

33 SWOT, BIKER is better at explaining the temporal variation of gas exchange (median correlation

34 coefficient of 0.91), than reproducing the absolute rates of exchange (median normalized RMSE

35 of 37%). Finally, BIKER is robust to measurement errors implicit in the SWOT data. Upon

36 SWOT's launch, we suggest that BIKER will be useful in mapping global-scale fluvial gas

37 exchange and improving CO_2 emissions estimates when coupled with river CO_2 models.

1 Introduction

38

39   Natural systems play a critical role in the budgeting and accounting of the global carbon

40   cycle under climate change. Following Cole et al. (2007), the global river network is recognized

41   to emit substantial amounts of carbon to the atmosphere via evasion (gas exchange driven by

42   diffusion and near-surface turbulence at th air/water interface), in addition to their long understood

43   role in transporting carbon to the oceans via downstream advection. Current estimates of total

44   carbon dioxide evasion (FCO_2) to the atmosphere from the global river network vary from 650-

45   2000 Tg C/yr (Lauerwald et al., 2015; Liu et al., 2022; Raymond et al., 2013), with 167 Tg-C/yr

46   coming from mountain streams alone (Horgby et al., 2019). Despite rivers' small percentage of

47   the global land surface (0.67%- Liu et al., 2022), this carbon flux is on par with the total oceanic

48   CO_2 uptake rate (Gruber et al., 2019; Horgby et al., 2019) and the global forest carbon uptake rate

49   (Pan et al., 2011).

50   River CO_2 evasion is increasingly better constrained and is clearly a critical component of

51   the global carbon cycle. Equation 1 represents this riverine flux given δCO_2 (the air-water

52   difference between the water $CO_{2_{water}}$ and the air $CO_{2_{air}}$) and the gas exchange velocity k. Consult

53   Appendix A for variable nomenclature used throughout this study.

$$FCO_2 = k\delta CO_2 (1)$$

54

55   There is a robust existing literature exploring spatiotemporal patterns in $\delta CO_{2_{water}}$ (e.g.

56   Aho, Fair, et al., 2021; Aho & Raymond, 2019; Crawford et al., 2017; Liu & Raymond, 2018;

57   Peter et al., 2014; Ran et al., 2017; Raymond et al., 2000; Rocher-Ros et al., 2019). This work has

58   lead to recent river-reach explicit modeling of δCO_2 using global hydrography datasets at up to

59   monthly temporal resolutions (Brinkerhoff et al., 2021; Horgby et al., 2019; Liu et al., 2022;

60   Saccardi & Winnick, 2021), but an equivalently sophisticated representation of k_{CO_2} is still

61   lacking.

62   The structure of Equation 1 necessitates that calculations of FCO_2 are highly sensitive to

63   measurements/estimates of k. However, k can only be directly calculated via a known gas flux,

64   eddy-covariance measurements, or tracer additions to the stream (Hall & Ulseth, 2020). In trying

65   to constrain the global fluvial FCO_2 flux across millions of rivers, this calculation is impossible

66   and necessitates the use of predictive models for k that are based on easily obtained river hydraulic

67   properties. In that vein, there have been over 20 empirical models developed to predict k from river

68   hydraulics, generally using some combination of mean velocity $\bar{U}$, shear velocity U_*, width W,

69   depth H, and slope S as predictors (Hall & Ulseth, 2020; Wang et al., 2021). These models usually

70   predict k_{600}, or k normalized by a Schmidt number (*Sc*) of 600. This is to remove the effect of

71   water temperature and gas type from predictive models, as warmer waters and lower *Sc* numbers

72   each increase gas exchange rates (Hall & Ulseth, 2020). Specifically, k_{600} reflects the k_{CO_2} at 20

73   degrees Celsius. Through this normalization, these models focus solely on physical explanations

74   for variation in k (Hall & Ulseth, 2020).

75   Applying these k models across watersheds, regions, or continents is called 'upscaling.'

76   This upscaling allows for estimating the difficult-to-measure k term in Equation 1 for any arbitrary

77   number of rivers, but also changes the base parameters that ultimately control the final estimate of

78   FCO_2. That is, by making k a function of hydraulics, $FCO_{2_{upscaled}}$ is now a direct function of river

79   hydraulics. This functional relationship is described in equation 2. It suggests that FCO_2 estimates

80   are not only at the mercy of the accuracy and spatiotemporal resolution of δCO_2, but also the

81   accuracy and resolution of our river hydraulics estimates.

82    $$FCO_{2_{upscaled}} = f\left(k_{CO_2}, \delta CO_2\right) = f(\bar{U}, H, S, W, \delta CO_2)(\mathbf{2})$$

83   Global upscaling has been performed in the literature. Raymond et al. (2013), Lauerwald

84   et al. (2015), and Horgby et al. (2019) all relied on k_{CO_2} values indirectly estimated using mean

85   annual streamflow models and hydraulic scaling equations to predict the hydraulic terms to in turn

86   predict k_{CO_2}, while Borges et al. (2015) used a combination of the above method and a constant

87   k_{CO_2} in space and time to upscale over Africa. More recently, Liu et al. (2022) performed a first

88   upscaling assessment of monthly temporal dynamics in global river FCO_2, though they relied on

89   monthly modeled streamflow and used the same model for k_{600} as previous studies (Raymond et

90   al., 2013) to achieve this. In all of these foundational studies, the temporal dynamics of k_{CO_2} (and

91   thus dynamics in FCO_2) were ignored because of hydraulic data limitations. It has been shown at

92   the field-scale that temporal dynamics of gas exchange can vary widely from site to site (Wallin

93   et al., 2011), but it has remained impractical to obtain temporally explicit k_{CO_2} at continental-to-

94   global scales.

95   Wang et al. (2021) recently attempted to address this global k problem by simulating k_{O_2}

96   in 35 rivers of many sizes (widths ranging from 0.23–349m) using a stream metabolism model

97   (Appling et al., 2018) and in situ dissolved oxygen (DO) datasets to infer what k_{O_2} must have been

98   to produce their 'observations'. They then compared this simulated dataset against direct

99   measurements of k, finding similar performance and parameter values for process-based models

100   of gas evasion. However, they were still limited by a lack of direct hydraulic measurements and

101   had to rely on hydraulic scaling equations to estimate river depth and velocity. Even though

102   approaches like Wang et al. (2021)'s are incredibly useful for expanding our mechanistic

103   understanding of gas exchange, they are less useful for global upscaling purposes as they rely on

104   high fidelity in situ DO data for every river (Hall & Ulseth, 2020).

105   We have established that literature has a reasonably good understanding of δCO_2 and a

106   relatively poorer understanding of k_{600} (and therefore k_{CO_2}) across large areas and in time. In

107   theory, the discrepancy between the quality of our $\delta CO_{2_{water}}$ and k_{CO_2} estimates could be

108   alleviated if direct hydraulics measurements (and in turn k_{CO_2} via Equation 2) were available at

109   the global scale at a sufficient temporal resolution. Spatially and temporally dynamic hydraulic

110   measurements in turn would also address the uncertainty regarding continental-to-global scale

111   temporal dynamics of gas exchange noted earlier.

112   Conveniently, these hydraulic data will soon be available via the upcoming

113   NASA/CNES/UKSA/CSA Surface Water and Ocean Topography (SWOT) satellite mission.

114   SWOT is expected to launch in late 2022 and provide the world's first direct measurements of

115   global water surface extent and elevation (and therefore water surface slope) at novel temporal

116   resolutions. SWOT is a wide swath radar interferometer and will sample rivers every 1 to 7 days

117   per 21 day repeat cycle, measuring rivers wider than 100m with a goal of expanding this to rivers

118   at least 50m wide (Biancamaria et al., 2016). Via its direct hydraulic measurements, SWOT is

119   expected to usher in a sea change in global-scale hydrology, and could similarly influence fluvial

120   biogeochemsitry if techniques are developed to ingest SWOT data and infer k. In this context, we

121   borrow tools from fluvial geomorphology and existing SWOT algorithms to answer the following

122   two questions:

123   1)   Can we develop a physically-based hydraulic model for k_{600} unique to SWOT-observed

124   rivers?

125   2)   Can we exploit such a model to infer k_{600} (and its uncertainty) solely from SWOT

126   observations?

127   To answer this first question, we use hydraulic geometry- the fundamental geomorphic

128   relationships between streamflow and channel shape (Gleason, 2015; Leopold & Maddock, 1953)

129   to develop a process-based model for large-river k_{600} (here defined as wider than 50m to align

130   with SWOT). We then take these findings and explore the second question by implementing this

131   hydraulic model, which defines k_{600}, within an algorithm named BIKER ('Bayesian Inference of

132   the k_{600} Evasion Rate') to infer k_{600} solely from SWOT measurements. The goal of BIKER is to

133   require no in situ inputs of any kind (although in situ data could be ingested and would improve

134   results) such that it is globally implementable on any SWOT-observable river. We validate BIKER

135   on 47 SWOT-simulated rivers (as SWOT has not yet launched) and explore BIKER's robustness

136   to the expected measurement errors implicit in the satellite's observations. Finally, we also couple

137   BIKER's k_{600} estimates with δCO_2 to predict gas fluxes and compare these against established

138   literature methods that rely on in situ hydraulic measurements.

139   This paper is split into two distinct parts: gas-exchange theory/model development (Section

140   2) and BIKER algorithm development/validation (Section 3). Section 3 is fundamentally

141   dependent on the results presented in Section 2, therefore Section 2 presents both theory and

142   results. Both sections detail the data used. We conclude with a discussion (Section 4) that

143   encompasses both gas exchange theory and remote sensing. Figure 1 conceptually maps out the

144   algorithm's approach to inferring k_{600} from SWOT data.

145
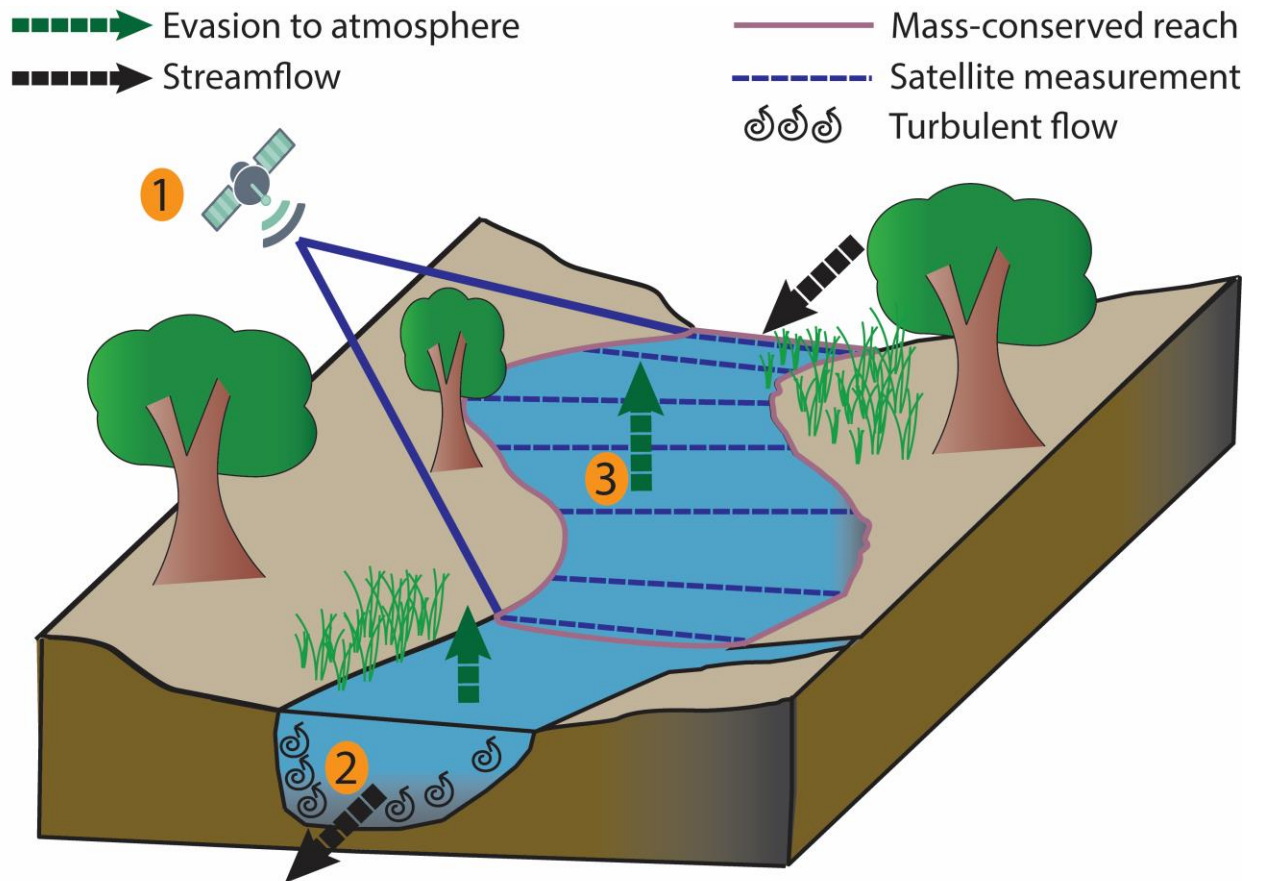
146   *Figure 1: Conceptual overview of the BIKER algorithm. 1: SWOT will directly measure*

147   *water surface width and elevation (and thus slope) at a series of cross-sections within mass-*

148   *conserved river reaches. 2: These hydraulics measurements are used to calculate turbulent*

149   *dissipation in the river channel (Section 3). 3: Turbulent dissipation is used to infer k_{600} via a*

150   *process-based model (Section 2).*

151   **2 Predicting k_{600} from large-river hydraulic geometry**

152   To predict k_{600} in the large rivers that SWOT will observe, we start from an established

153   process-based model for k_{600}, impose hydraulic assumptions that are valid in SWOT-observable

154   rivers, and obtain a model we empirically test. Following a description of the data (Section 2.1),

155   we outline established models (Section 2.2) and then step through our hydraulic assumptions to

156   arrive at an equation that is compatible with SWOT measurements (Section 2.3). We then

157   empirically validate the model (Section 2.4)

158   **2.1 Data**

159   We develop our hydraulic model for k_{600} using multiple datasets of measured k_{600} and

160   stream hydraulics collected from the literature. In total, we obtain 763 measurements of k_{600}, with

161   701 of these measurements previously gathered by Raymond et al. (2012) and Ulseth et al. (2019).

162   The remaining measurements come from Churchill et al. (1964) and Owens et al. (1964). See Table

163   S1 for a complete list of the studies that collected these measurements. All k_{600} measurements

164   come from tracer studies and thus define k_{600} at the reach scale.

165   In addition to hydraulics measured alongside k_{600} and reported above, we expand our

166   dataset of stream hydraulics using a previously published compilation of in situ hydraulic

167   measurements (Brinkerhoff et al., 2019). That dataset contains over 530,000 unique measurements

168   of river channel velocity, width, and discharge from across the continental United States, originally

169   made to calibrate United States Geological Survey (USGS) stream gauge rating curves and made

170   public by the USGS. This dataset is used to calculate how frequently SWOT observable rivers

171   meet our large-river hydraulic assumptions (Section 2.3).

2.2 Process-based hydraulic modeling of river k

173   k scales with near-surface turbulence in turbulent streamflows (Hall & Ulseth, 2020), and

174   extensive field and laboratory experiments have converged on the 'small-eddy model' for k as

175   derived by Lamont & Scott (1970) and empirically anticipated by Calderbank & Moo-Young

176   (1961). This model scales k via the smallest-scale turbulent eddies and has been repeatedly

177   empirically validated in freshwater systems (e.g. Katul et al., 2018; Lorke & Peeters, 2006; Moog

178   & Jirka, 1999b; Tokoro et al., 2008; Vachon et al., 2010; Wang et al., 2021; Zappa et al., 2003,

179   2007). The small-eddy model is provided as Equation 3, where ϵ is the dissipation rate of near-

180   surface turbulence, v is the kinematic viscosity, and Sc is the Schmidt number.

181    $$k \propto Sc^{-1/2}(v\epsilon)^{1/4} \quad \textbf{(3)}$$

182   Some laboratory and field observations additionally suggest that open channel flows with

183   small bed roughness do not exhibit homogeneous surface dissipation across the entire reach's air-

184   water interface (Moog & Jirka, 1999a; Talke et al., 2013). Given this observation, Moog & Jirka

185   (1999a) proposed an extension to the small-eddy model, additionally scaling k_{600} using a shear

186   Reynold's number Re_* formulation. This is Equation 4 and is referred to here as the 'Reynolds

187   extension' model. The Reynolds model is hypothetically useful in low-turbulence scenarios where

188   a relative lack of large-scale eddies effectively 'filter out' the number of small-eddies that actually

189   reach the interface and initiate gas exchange (Talke et al., 2013). While scaling k via a shear

190   Reynold's formulation is sometimes done to parameterize wave-breaking gas exchange models in

191   the open ocean (e.g. Brumer et al., 2017; Zhao et al., 2003; Zhao & Toba, 2001), it is infrequently

192   done in rivers. In the context of BIKER, we chose to test this model because large, SWOT-

193   observable rivers are generally the smoothest, least-turbulent flows along the stream-to-ocean

194   continuum where small eddies might not reach the surface. Further, to our knowledge, this

195   Reynolds extension model has never been empirically tested in predicting river k, aside from

196   confirming that large-scale eddies differentially move turbulence to the surface in a large river

197   (Talke et al., 2013).

$$k \propto Sc^{-1/2}(v\epsilon)^{1/4}(Re_*)^{3/8} \quad (\mathbf{4})$$

198

199   Equations 3 and 4 both rely on ϵ, which is non-trivial to measure. When working at large

200   scales, a commonly used ϵ model assumes that all turbulence is generated at the bed and

201   transported to the air-water interface via the log-law-of-the-wall (Equation 5). Another approach

202   specific to fluvial settings models k via 'form-drag dissipation' (Equation 6) which is equivalently

203   the total stream power per unit mass water. This normalized stream power captures the bulk

204   frictional resistance (and thus energy dissipation) via channel banks, meanders, bars, etc. that is

205   unique to fluvial systems (Moog & Jirka, 1999b). Authors have since shown that Equation 6 can

206   reasonably predict k in rivers and streams (Raymond et al., 2012; Ulseth et al., 2019; Wang et al.,

207   2021).

208
$$\epsilon = \epsilon_S = \frac{U_*^3}{H} \text{ (5)}$$

209
$$\epsilon = \epsilon_D = gS\bar{U} \text{ (6)}$$

210 **2.3 Deriving a large-river k_{600} model**

211 Given the theoretical context provided in Section 2.2, we now turn to SWOT-observable

212 systems specifically. Rivers and streams change predictably along their longitudinal profile from

213 source to sea, and we can exploit the hydraulic geometry of large rivers at the end of this continumn

214 to estimate k in SWOT rivers. In general, as river size increases, channels become more

215 rectangular, their shapes elongate (becoming wider quicker than they become deeper) and their

216 hydraulic radii begin to approximate their mean flow depth, i.e. $R_h \approx H$ (Leopold & Maddock,

217 1953). This is a common assumption in hydraulic and geomorphic modeling of large rivers. For

218 example, SWOT-observable river flows have an average $\frac{R_h}{H}$ ratio of 0.98 and standard deviation of

219 only 0.02 (n = 22452; see Text S1 for how we built this dataset). We refer to these rivers as

220 'hydraulically-wide'.

221 We therefore assume that all SWOT-observable rivers are hydraulically-wide to derive a

222 model for gas exchange. The overall goal is to reduce the equations down to their fundamental

223 parameters, identifying which terms are SWOT observable and limiting the number of terms not

224 directly measurable via SWOT. To do this, we impose $\epsilon = \epsilon_D$ and $R_H = H$ on the Reynolds

225 extension model (Equation 4) and arrive at Equation 7 (with statistical coefficient β_1). Equation 7

226 thus defines gas exchange velocity solely as a function of slope, mean flow depth, and mean flow

227 velocity. This is theoretically valid only in a hydraulically-wide channel.

228
$$k_{600} = \beta_1 (gS)^{7/16} \bar{U}^{1/4} H^{9/16} \qquad (\mathbf{7})$$

229   We also test the performance of three other models for predicting k in hydraulically-wide

230   channels via the other three unique combinations of Equations 3-4 and Equations 5-6. While the

231   complete model derivations and results for all four models are provided in Text S2 and Figure S1,

232   the final and best-performing model (Equation 7) is presented and used below.

233   **2.4 Model validation**

234   With Equation 7 derived, we now empirically test its strength of fit in hydraulically-wide

235   river flows. We validate on the dataset of in situ measurements of k_{600}, after filtering for

236   measurements made in hydraulically-wide channels, which was defined as flows whose hydraulic

237   radius was within 1% of their mean flow depth. All told, this amounts to 166 measurements of

238   hydraulically-wide k_{600}. Equation 7 is assessed via the coefficient of determination (r^2) and

239   plotted in Figure 2. Note that Figure 2 axes are plotted in logarithmic space only for visualization:

240   model fit and validation (via r^2) were calculated in linear space as their models dictate.
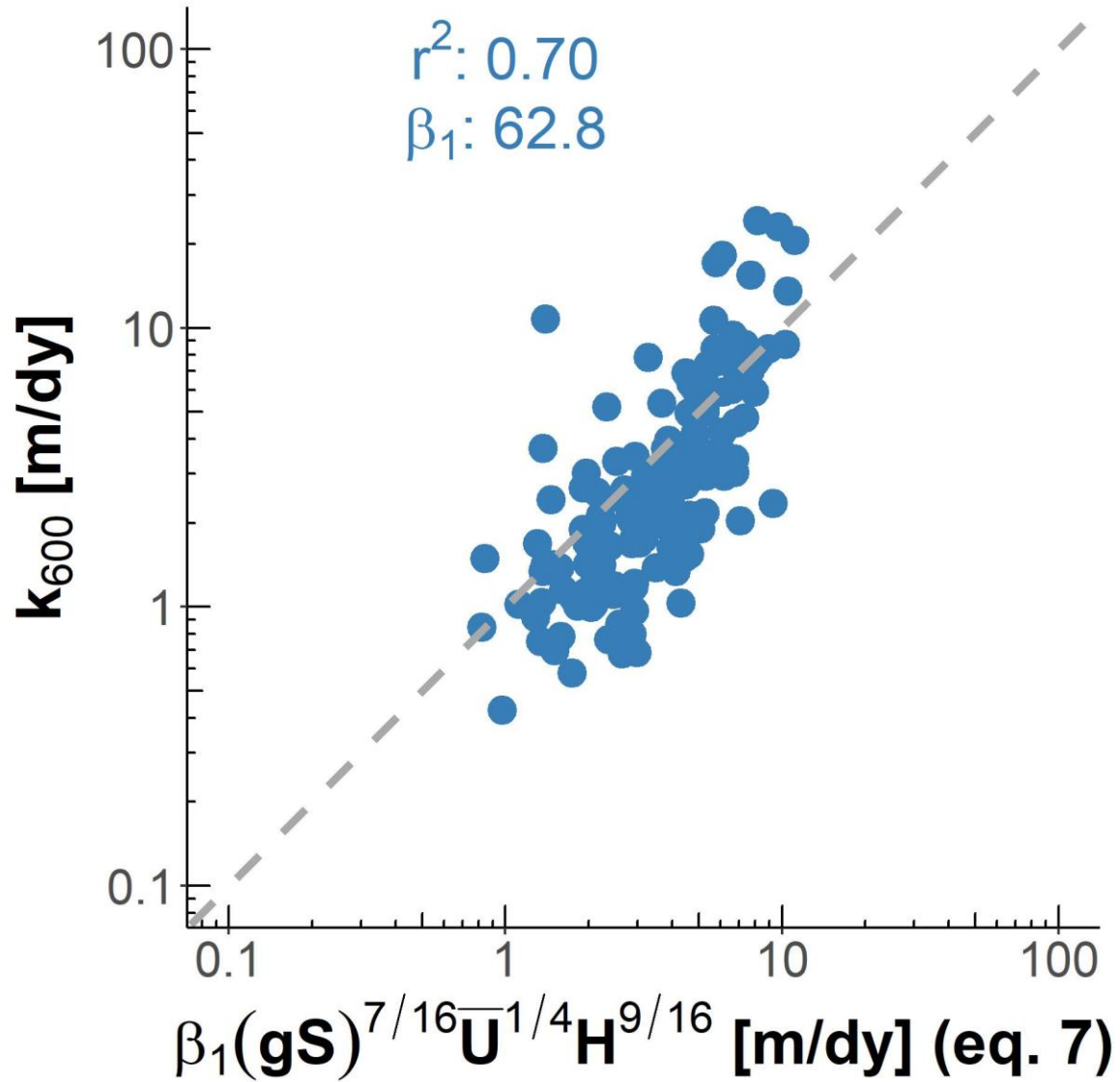
241

Figure 2: Empirical testing of our large-river k_{600} model on 166 measurements made in hydraulically-wide rivers. Dashed grey line denotes the 1:1 line. Note that axes are plotted in logarithmic space just for visualization: model fit and validation (via the coefficient of determination r^2) were calculated in linear space.

246   Figure 2 shows that Equation 7 explains 70% of variation in observed k_{600} in hydraulically-

247   wide rivers and accurately captures the scaling dynamics of observed k_{600} as well. The value for

248   β_1 is 62.8, which is similar to the fitted parameters in other Re_* and U_* models for river k (Wang

249   et al., 2021). While the individual residuals can be quite large, the overall scaling of k_{600} with

250   river hydraulics is strongly captured, remembering that Figure 2 is plotted in logarithmic space.

251   Compared to other combinations of Equations 3-6 (Figure S1), there is also a better fit with the

252   estimates thanks to the addition of the Reynold's number scaling for low-turbulent flows (as

253   expected). The success of this model in hydraulically-wide channels provides us with a strong

254   physical-model for gas evasion built with SWOT in mind. The river hydraulics terms in Equation

255   7 ($\bar{U}$, H, and S) can either be directly measured or reasonably inferred from SWOT measurements,

256   effectively opening the door for remotely sensing the gas exchange velocity.

257   **3 Exploiting Equation 7 to remotely sense gas exchange velocity**

258   We have shown that scaling k_{600} via Equation 7 is useful in hydraulically-wide rivers.

259   Further, Equation 7 has only three non-directly-remotely-sensible terms: k_{600}, mean flow depth,

260   and mean flow velocity. Conveniently, techniques to simultaneously infer mean flow depth and

261   velocity from SWOT data (among other parameters) have been established over the last decade to

262   infer streamflow from SWOT's measurements (e.g. Andreadis et al., 2020; Brinkerhoff et al.,

263   2020; Brisset et al., 2018; Durand et al., 2014; P.-A. Garambois et al., 2020; P.-A. Garambois &

264   Monnier, 2015; Gleason et al., 2014; Gleason & Smith, 2014; Hagemann et al., 2017; Larnier et

265   al., 2020; Oubanas et al., 2018). For BIKER, we follow the work developed by Hagemann et al.

266   (2017), Brinkerhoff et al. (2020), and Durand et al. (2014) to infer k_{600}, channel depth and velocity

267 from SWOT observations using a modified form of Manning's equation. Following a description

268 of the data used (Section 3.1), we detail algorithm development and experimental design (Section

269 3.2) and then we present the validation results (Section 3.3).

270   **3.1 Data**

271   To validate BIKER, we cannot use actual SWOT measurents as SWOT has yet to

272 launch. In the hydrology literature, it has become standard practice to benchmark SWOT-related

273 algorithms on "SWOT-like" data (Durand et al., 2016). We use 47 SWOT-simulated rivers for

274 validation, where these simulated rivers are simply reach-averaged hydraulic model outputs where

275 the water surface heights, slopes, and widths are labelled as RS observations and are used as the

276 sole inputs to BIKER. These datasets are created using standard hydraulic models forced with

277 known inflows and measured bathymetry to model the hydraulic response of the rivers, and then

278 those terms visible to SWOT are extracted to produce hydraulically realistic synthetic

279 observations. These data were published by Frasson et al. (2021) and Durand et al. (2016). See

280 Figure S2 for a map of these river's locations along the global SWOT river network (Altenau et

281 al., 2021). This river network corresponds to every river that BIKER will be run on once SWOT

282 launches.

283   We validate BIKER under two different 'error scenarios' (section 3.2.2). While SWOT

284 will provide river surface measurements of novel quality and resolution, as with all remote sensing

285 products there are expected errors that will be implicit in these measurements. Here, we validate

286 BIKER under a 'no-measurement-error' scenario that reflects an unrealistic measurement as if

287 SWOT has perfect accuracy and precision: we use the hydraulic model output directly as a first

288   test of algorithm validity. 16 of these rivers are then additionally validated under a 'measurement-

289   error' scenario that more closely mimics expected SWOT by adding realistic radar errors and

290   sampling along the satellite's future ground track. SWOT river error modeling was developed by

291   Durand et al. (2020) and then applied to these 16 rivers by Frasson et al. (2021). This error

292   modelling is non-trivial and computationally expensive, and thus we rely on these previously

293   published data.

294   For CO_2 evasion and carbon emissions calculations, we use 26 bi-weekly dissolved CO_2

295   samples collected by Beaulieu et al. (2012) at one location in the Ohio River (Figure S2) for one

296   calender year from 2008-2009 (Figure S3). Note that this CO_2 data is for the Ohio River only but

297   was applied to all rivers to provide a physically realistic signal for CO_2 fluxes with meaningful

298   seasonality and dynamics. Therefore, the raw carbon emissions estimates presented in this paper

299   are meaningless in the context of actually measured carbon emissions from these rivers, but are

300   better than specifying CO_2 concentrations devoid of context. These data are necessary as we are

301   interested in the effect of BIKER k_{600} errors on eventual fluxes and comparing these fluxes with

302   published methods. Therefore, applying these 'unit' CO_2 values allows for such a comparison by

303   providing a realistic timeseries.

304   **3.2 Section 3 methods**

305   **3.2.1 BIKER**

306   BIKER, and Bayesian inference in general, starts from Bayes rule (Equation 8), where $\varTheta$

307   is some set of non-remotely-sensible parameters we want to solve for (including k_{600}), x is the

308 observed data, $f(x|\Theta)$ is the sampling model where data are conditional on the parameters, and

309 $p(\Theta)$ is the joint prior distribution of the parameters. Therefore, we are interested in solving for

310 $p(\Theta|x)$, or the 'posterior' distribution. Note that $p(x)$ is usually computationally intractable to

311 integrate exactly, but Bayesian inference requires only the proportionality to be specified:

312 $p(\Theta|x) \propto f(x|\Theta)p(x)$. Sampling algorithms are then used to approximate the actual posterior

313 distribution, as is done in BIKER.

314
$$p(\Theta|x) = \frac{f(x|\Theta)p(\Theta)}{p(x)} \ (\mathbf{8})$$

315 The heart of BIKER is its reformulation of the k_{600} model (Equation 7) as a Bayesian

316 sampling model that is conditional on the non-remotely-sensible parameters (i.e. $f(x|\Theta)$). This is

317 similar to the 'McFLI' (Mass-Conserved Flow Law Inversion) logic used in some SWOT RSQ

318 algorithms (Gleason et al., 2017). To start, we write k_{600} as a function of SWOT-observables W

319 and S. This algebra is carried out using Equation 7, the fitted value for β_1 from Figure 2 (62.82),

320 and Manning's equation for mean flow velocity ($\bar{U} = \frac{1}{n}R_h^{2/3}S^{1/2}$). Following Section 2.3, we

321 continue to assume that the channel is hydraulically-wide ($R_h = H = \frac{A}{W}$). To leverage additional

322 SWOT data, the wetted channel area A is further split into the the SWOT-unobservable portion A_0

323 and SWOT-observable portion dA following Durand et al. (2014) and Hagemann et al. (2017)

324 where $dA_{it} = \sum_{t':W_{t'} \leq W_t} W_{t'}\delta H_{e_{t'}}$, for cross-section i and timestep t within a mass-conserved river

325 reach.

326   All of this algebra simplifies to Equation 9. Conveniently, k_{600} as measured by tracer

327   additions to a stream is inherently a reach-scale quantity (in a mass-conserved reach). Therefore,

328   Equations 7 and 9 both yield a reach-scale k_{600} (i.e. $k_{600_i} = k_{600} \forall i$). This lowers the number of

329   parameters BIKER must infer and makes the problem much better constrained.

330
$$k_{600_t} = 62.82 g^{7/16} S_{it}^{9/16} \frac{1}{n_i}^{1/4} \left(\frac{A_{0_i} + dA_{it}}{W_{it}} \right)^{35/48} \textbf{(9)}$$

331   Next, Equation 9 is written as a Bayesian sampling model, in which all of the SWOT

332   observations are sampled from the unknown model parameters (A_{0_i}, k_{600_t}, and n_i). This is

333   Equation 10 after describing everything as normal distributions of the log-transformed terms. $\sigma_{k_{600}}^2$

334   refers to the total uncertainty implicit in Equation 9. This uncertainty arises from 1) parameter

335   uncertainty in Equation 7, 2) Manning's equation, and 3) the rectangular channel assumption.

336    $\left[log(62.82) + \frac{7}{16} log(g) + \frac{9}{16} log(S_{i,t}) - \frac{35}{48} log(W_{i,t}) \right] \sim \mathcal{N} \left(\left[log(k_{600_t}) + \frac{1}{4} log(n_i) - \frac{35}{48} log(A_{0_i} + dA_{i,t}) \right], \sigma_{k_{600}}^2 \right) \textbf{(10)}$

337   Equations 8 and 10 also necessitate that we specify prior distributions for the parameters

338   A_{0_i}, k_{600_t}, and n_i. Prior distributions formalize the a priori estimates and uncertainties for the non-

339   remotely-sensed terms. More intuitively, BIKER priors represent our 'prior river knowledge' of

340   what A_{0_i}, k_{600_t}, and n_i probably are for some river since they cannot be directly remotely sensed.

341   This is analogous to the 'empirical Bayes approach' to Bayesian inference (Hoff, 2009). Our goal

342   in prior specification was to rely on absolutely no in situ information such that we could run this

343   method on any river on Earth solely using SWOT observations. In theory, more informed priors

344   via various a priori information about a specific river will improve BIKER performance, but here

345   we chose to test the fully generalized algorithm. Therefore, the validation presented here is a

346   'worst-case scenario', wherein BIKER performance should improve with better prior information

347   on the river. In that context, we used a variation of the prior specification method developed by

348   Brinkerhoff et al. (2020), who developed 'geomorphic river types' with distinct prior sets for A_{0_i}

349   and n_i. These priors are assigned to a river solely using SWOT data *W* and *S*, therefore meeting

350   our needs for complete global implementability. Prior assignment for k_{600_t} was developed

351   similarly (all prior specifications are elaborated on in Text S3).

352   With the sampling model described ($f(x|\theta)$ = Equation 10) and priors $p(x)$ specified (Text

353   S3), a joint posterior distribution conditional on the SWOT observations ($p(\theta|x) \propto f(x|\theta)p(x)$)

354   is therefore also specified. To approximate this distribution, we use a Markov Chain Monte Carlo

355   (MCMC) algorithm implemented using the Stan probabilistic programming language.

356   Specifically, Stan uses a Hamiltonian Monte Carlo sampler which reduces computation time

357   relative to other sampling algorithms (Hagemann et al., 2017).

358   **3.2.2 BIKER validation**

359   We validate BIKER, assuming no measurement error, on 47 SWOT-simulated rivers using

360   daily simulated hydraulics. We also re-validate BIKER under the 'measurement-error' scenario

361   using the 16 rivers with Frasson et al. (2021)'s SWOT error model to corrupt the hydraulics to

362   mimic realistic SWOT measurements (widths, heights, and slopes). These data were outlined in

363   Section 3.1.

364   BIKER is unique in that it can provide a timeseries of k_{600}: for each SWOT observation,

365   it yields a unique k_{600}. There are, to our knowledge, no datasets of k_{600} over time approaching

366   the temporal density of our simulated SWOT rivers. We therefore apply Equation 7 as validated

367   in Figure 2 to specify k_{600} given the true hydraulics of each case and compare BIKER's inversion

368   to that value: given observed hydraulics, 'observed' k_{600} comes from Equation 7. Remember that

369   SWOT cannot observe below the water surface and therefore cannot measure $\bar{U}$ or H (hence the

370   need for Equation 9), and that all SWOT observations contain errors in both space and time (hence

371   Equation 10). We acknowledge that there is error in Equation 7 as shown in Figure 2, but this error

372   can be explicitly parameterized in our Bayesian system (this is elaborated on in Text S4).

373   Therefore, the BIKER validation presented here is an exercise to see how well the imperfect and

374   partial SWOT observations can infer k_{600} given the hydraulic assumptions in Equation 9 and

375   uncertainty in the data itself. Note also that we have already empirically validated Equation 7 in

376   Figure 2.

377   We validate BIKER as a timeseries of k_{600} for each river using the BIKER posterior means.

378   Our error metrics consider the timeseries nature of the problem and are formally defined in Table

379   1. They consist of the correlation coefficient r to quantify accuracy of BIKER's temporal

380   dynamics, the root mean square error normalized by the observed mean (NRMSE) and normalized

381   mean absolute residual error (NMAE) to assess bias, and the Kling-Gupta Efficiency (KGE). KGE

382   is frequently used to assess streamflow prediction and simultaneously assesses accuracy in both

383   bias and dynamics. While a value greater than -0.41 means the model outperforms a uniform

384 prediction of the mean (Knoben et al., 2019), generally KGE scores are interpreted as being

385 meaningful in ungauged settings if > 0.

386   *Table 1: Validation metrics used in this study, where Nt is number of observations and i is*

387 *the specific observation. σ refers to the variance of the sample and μ refers to the mean of the*

388 *sample. Carrot accents indicate the predicted value.*

Description	Acronym	Definition	Ideal Score	Possible Range
Correlation Coefficient	r	$\sqrt{1 - \left(\dfrac{\sum_{i=1}^{N_t}\left(k_{600,i} - \widehat{k_{600_i}}\right)^2}{\sum\left(k_{600,i} - \mu_{k_{600}}\right)^2}\right)}$	1	-1 to 1
Normalized root-mean-square error	NRMSE	$\sqrt{\dfrac{1}{N_t}\sum_{i=1}^{N_t}\left(\dfrac{\widehat{k_{600_i}} - k_{600,i}}{\mu_{k_{600,i}}}\right)^2}$	0	0 to ∞
Kling-Gupta Efficiency	KGE	$1 - \sqrt{\left(r\left(k_{600_i}, \widehat{k_{600_i}}\right) - 1\right)^2 + \left(\dfrac{\mu_{\widehat{k_{600}}}}{\mu_{k_{600}}} - 1\right)^2 + \left(\dfrac{\sigma_{\widehat{k_{600}}}/\mu_{\widehat{k_{600}}}}{\sigma_{k_{600}}/\mu_{k_{600}}} - 1\right)}$	1	-∞ to 1
Normalized Mean Absolute Error	MAE	$\dfrac{\dfrac{\sum_{i=1}^{N_t}\left(\left|\widehat{k_{600_i}} - k_{600_i}\right|\right)}{n}}{\mu_{k_{600}}}$	0	0 to ∞

389   **3.2.3 Carbon emissions validation**

390   It is one thing to accurately model the temporal dynamics of k_{600} as above, but researchers

391 are often most interested in the actual carbon emitted from river to atmosphere. Per Equation 2,

392 this is done using river hydraulic models to estimate k_{CO_2} and in turn $FCO_{2_{upscaled}}$. However,

393 streamflow data and/or model outputs are more readily modeled at the global scale than river

394 channel geometry, and so upscaling models usually predict $\bar{U}$ and H as functions of streamflow

395 (Q) using hydraulic geometry scaling relationships. This effectively reduces Equation 2 to

396   Equation 11. It is worth stressing that these literature upscaling workflows rely on in situ

397   streamflow records and/or high-quality streamflow models.

398    $$FCO_{2_{upscaled}} = f(k_{CO_2}, \delta CO_2) = f(Q, \delta CO_2) \quad (\mathbf{11})$$

399   Conversely, BIKER represents a new way of approaching Equation 11 compared to

400   existing literature models: BIKER has no reliance on a streamflow model nor hydraulic geometry

401   scaling relationships and only requires that a river is SWOT-observable. We are therefore

402   interested in how the final carbon emissions that result from BIKER compare against literature

403   methods that use Equation 11. We have the data to test four different models for fluxes: 'BIKER',

404   'Raymond 2013', 'Raymond 2012', and 'Brinkerhoff 2019'. These latter three approaches all use

405   the same philosophy for k_{600}: making hydraulic and geomorphic assumptions to associate k_{600}

406   with observed hydraulics before using the CO_2 data as a realistic timeseries to yield fluxes per

407   Equation 11. In all three approaches, these observed hydraulics are streamflow, while BIKER uses

408   only SWOT observations. Therefore, the advantage of BIKER is in its ease of application, as

409   SWOT will observe all global rivers wider than 50m while streamflow observations are extremely

410   geographically limited. But, BIKER is only attractive if it can produce fluxes with similar errors

411   to published methods. Text S5 and Table S2 fully describe these three literature models.

412   To benchmark BIKER against these literature methods, we pair the 26 biweekly CO_2 and

413   water temperature samples from Beaulieu et al. (2012) (Section 3.1, Figure S3) with every 14th

414   set of daily SWOT observations (as the CO_2 data is bi-weekly). We then calculate FCO_2 using

415   Equation 1, an atmospheric $CO_{2_{air}}$ of 400 uatm, and a *Sc* estimated following Raymond et

416   al. (2012). The k in Equation 1 is obtained using BIKER or the three literature models (Table S2

417   and Text S5). Finally, we estimate a pseudo yearly total carbon emission rate (via CO_2 evasion)

418   by applying each river's mean FCO_2 over the river's surface area and summing all rates across

419   rivers, remembering that we are applying 'unit' CO_2 data to all rivers.

420   **3.3 Section 3 results**

421   **3.3.1 BIKER**

422   Figure 3 plots a representative set of the 47 timeseries of predicted and observed k_{600},

423   assuming no SWOT measurement error. Two rivers each were sampled from the three tertiles of

424   river *KGE* scores (Table 1) for display. Consult Figure S4 for all 47 timeseries plots (assuming no

425   measurement error) and Figure S5 for the 16 rivers with measurement errors. Note that the y axis

426   is normalized by maximum observed values to compare across rivers. In general, the temporal

427   dynamics of k_{600} are reproduced quite well by BIKER, with the highs and lows of evasion

428   correctly inferred by BIKER in the better-performing rivers. Notably, there is sometimes positive

429   bias in the estimates (e.g. the Connecticut and Missouri Midsection rivers). Some rivers yield the

430   correct temporal dynamics, but the magnitude of these values is stretched relative to the observed

431   (e.g. Ohio River). In this example, temporal trends are still reasonably inferred even though the
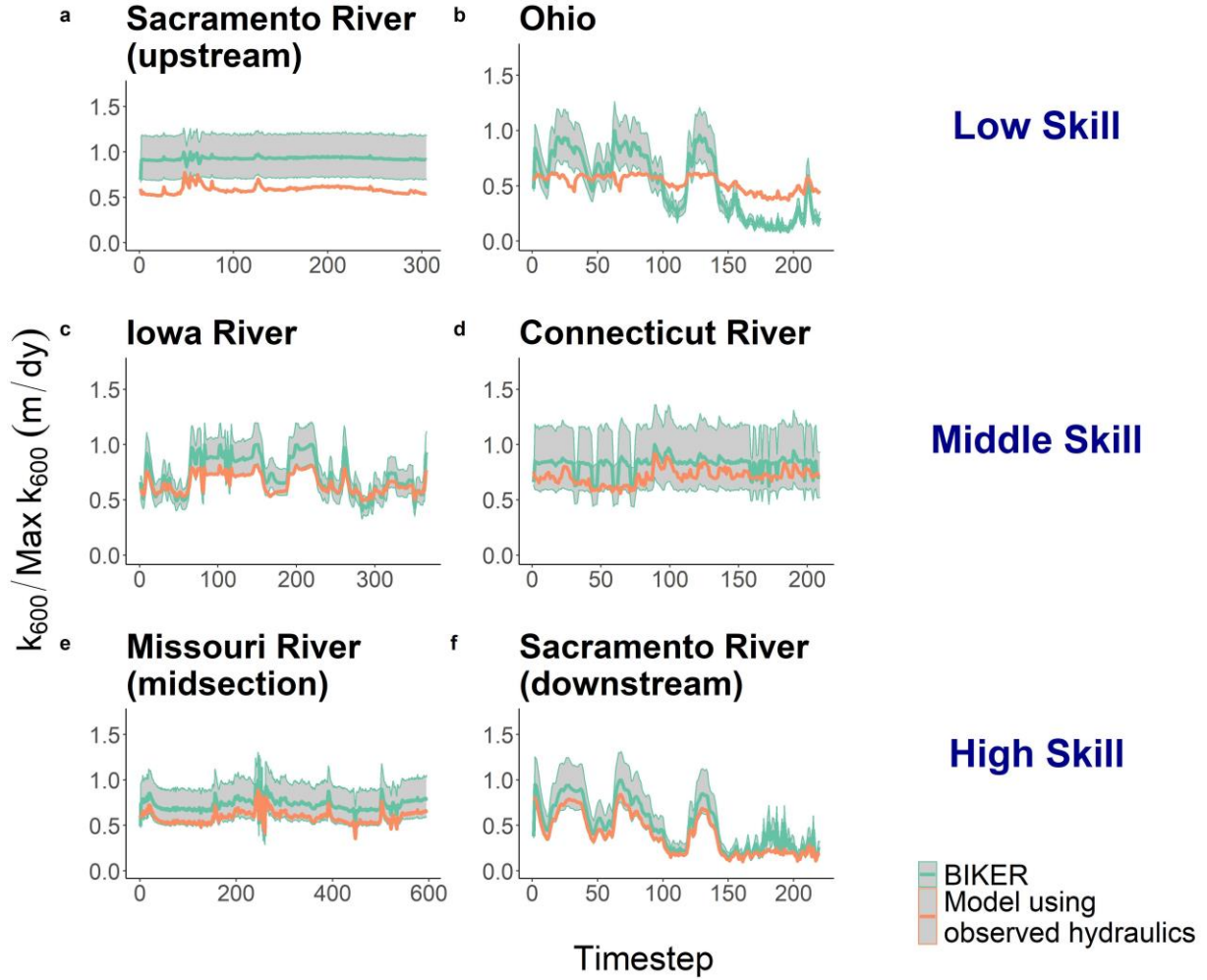
432   magnitude of the estimates is quite off.

Figure 3. Representative river timeseries plots of k_{600}. Orange is observed, while green is BIKER and uses SWOT measurements as its sole input. The green ribbon indicates the 95% CIs for the BIKER posteriors. Rivers are sampled from the three tertiles of KGE scores. (a-b) are poorest performing rivers, (c-d) are in the middle, and (e-f) are the best performing rivers. Y axis is normalized by maximum observed values to compare visually.

Next, we calculate performance metrics following Section 3.2.2 and Table 1. These are presented in Figure 4, which plots the scores for the 47 rivers with no measurement errors as

441   empirical cumulative density functions (eCDFs). Median river KGE is 0.37 and median river r is

442   0.91. Further, 38/47 rivers outperform a uniform prediction of the mean (KGE = -0.41). This

443   indicates strong inference of each river's temporal k_{600} dynamics given that absolutely no in situ

444   information is being used to predict k_{600}. NRMSE has a median score of 0.37, highlighting many

445   rivers which have notable positive biases (Figure 3 also confirms this visually). Median NMAE is

446   35%. Taken in aggregate, Figures 3-4 indicate that BIKER is quite good at capturing temporal

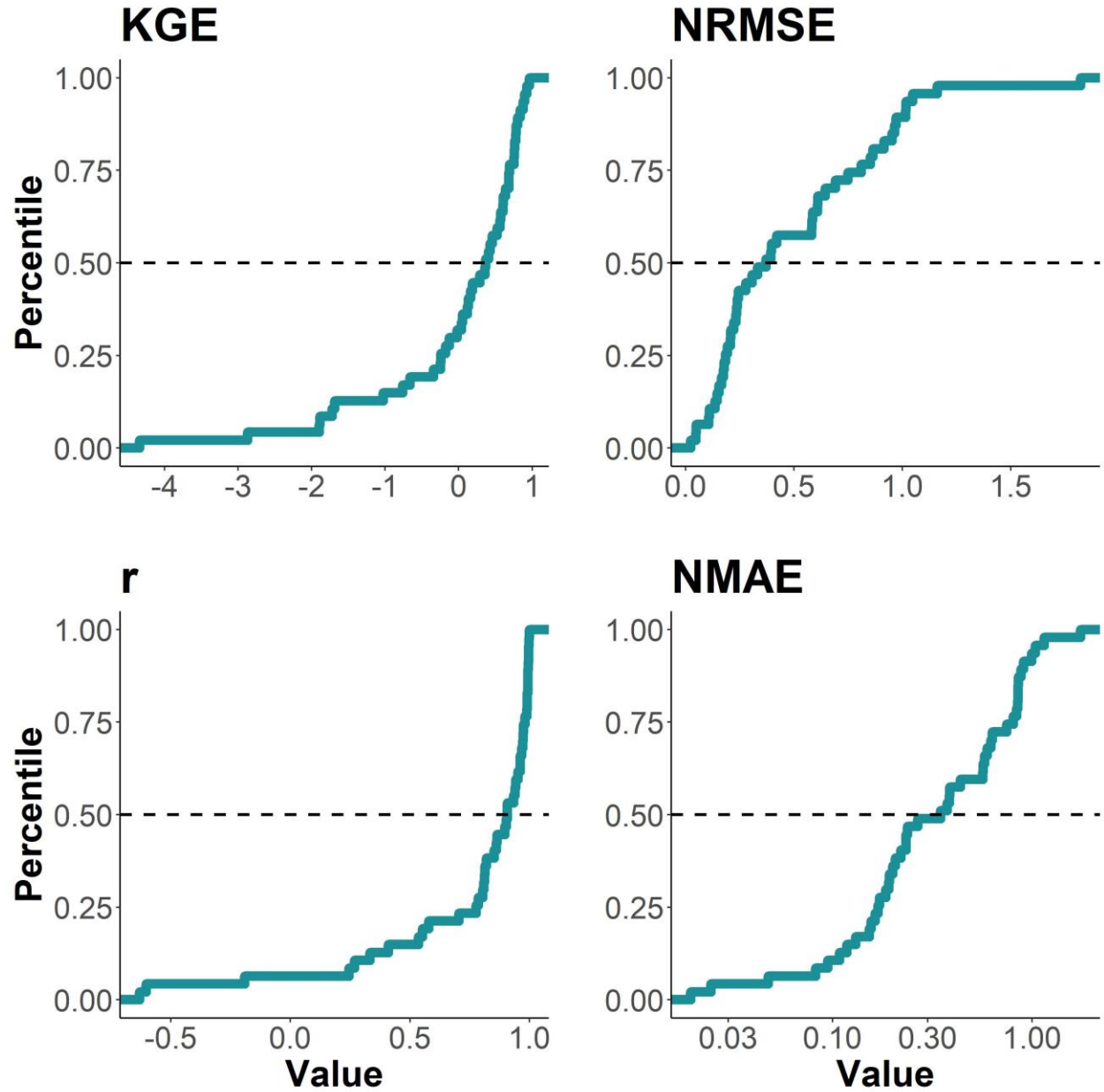447   dynamics in k_{600}, however there is often positive bias in its estimates.

448

449   *Figure 4. Performance metrics by river, ploted as empirical cummulative density functions*

450   *(eCDFs). Each subpanel is labelled by its performance metric (defined in Table 1). Dashed lines*

451   *denote median scores.*

452   Figure 5 compares BIKER results under the 'no-measurement-error' and 'measurement-

453   error' scenarios for the 16 rivers for which Frasson et al. (2021) provide an error model. Rivers

454   that fall within the purple zone get worse when accounting for measurement error, while rivers in

455   the green get better. Note also that axes are flipped in order to visualize all 'better performances'

456   in the upper-right-corner of each sub-plot. BIKER performs nearly identically, regardless of

457   implicit measurement errors in the inputs to the algorithm, i.e. points are scattered along the 1:1

458   line. Overall, these results strongly suggest that BIKER will be robust to the measurement errors

459   that will be implicit in SWOT's observations of river width and slope. Given these results, we

460   deem that SWOT measurement error does not exert a significant influence on BIKER performance

461   and so the results presented for the rest of the manuscript assume no measurement error in order

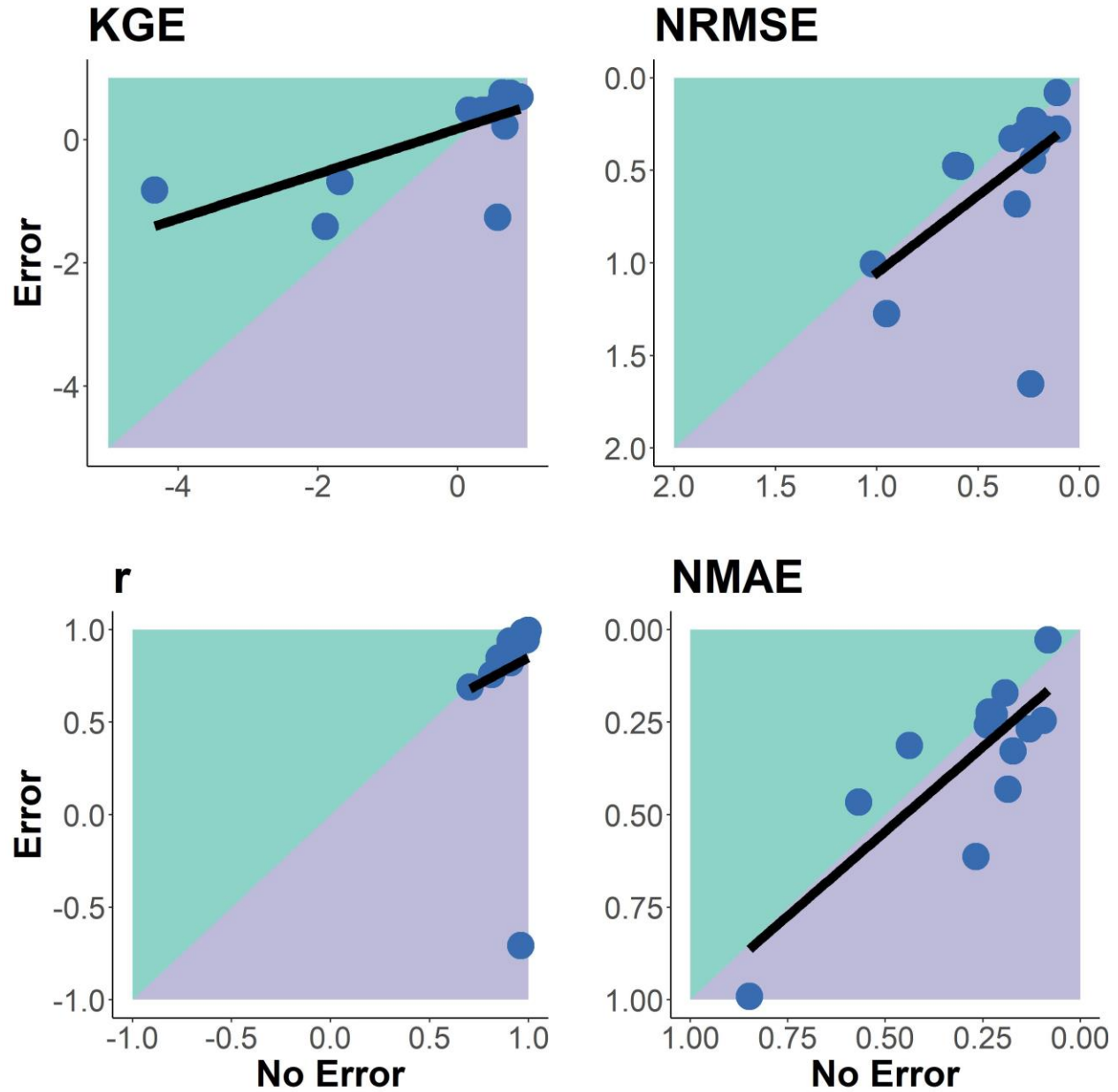462   to use all 47 rivers.

463

Figure 5: Comparison of BIKER performance when considering measurement error in the

SWOT observations for 16 rivers. Each subpanel is labelled by its performance metric (Table 1).

Rivers that fall within the purple zone get worse when accounting for measurement error, while

rivers in the green get better. Note that some axes are flipped in order to visualize all 'better

468   *performances' in the upper-right-corner of each sub-plot. Black line denotes linear regression to*

469   *aid in visualization.*

470   Finally, we sought to explore the overall influence of prior error/bias on k_{600}. We plot

471   eCDFs of prior and posterior NMAE (see Table 1 for metric definition) across all 47 rivers in

472   Figure 6a. Generally, errors/biases associated with the prior k_{600} are propagated through the

473   posterior in an approximately 1:1 manner (which is expected), except for a subset of rivers in

474   which posterior error actually increases relative to the prior (approximately percentiles 0.6-0.9).

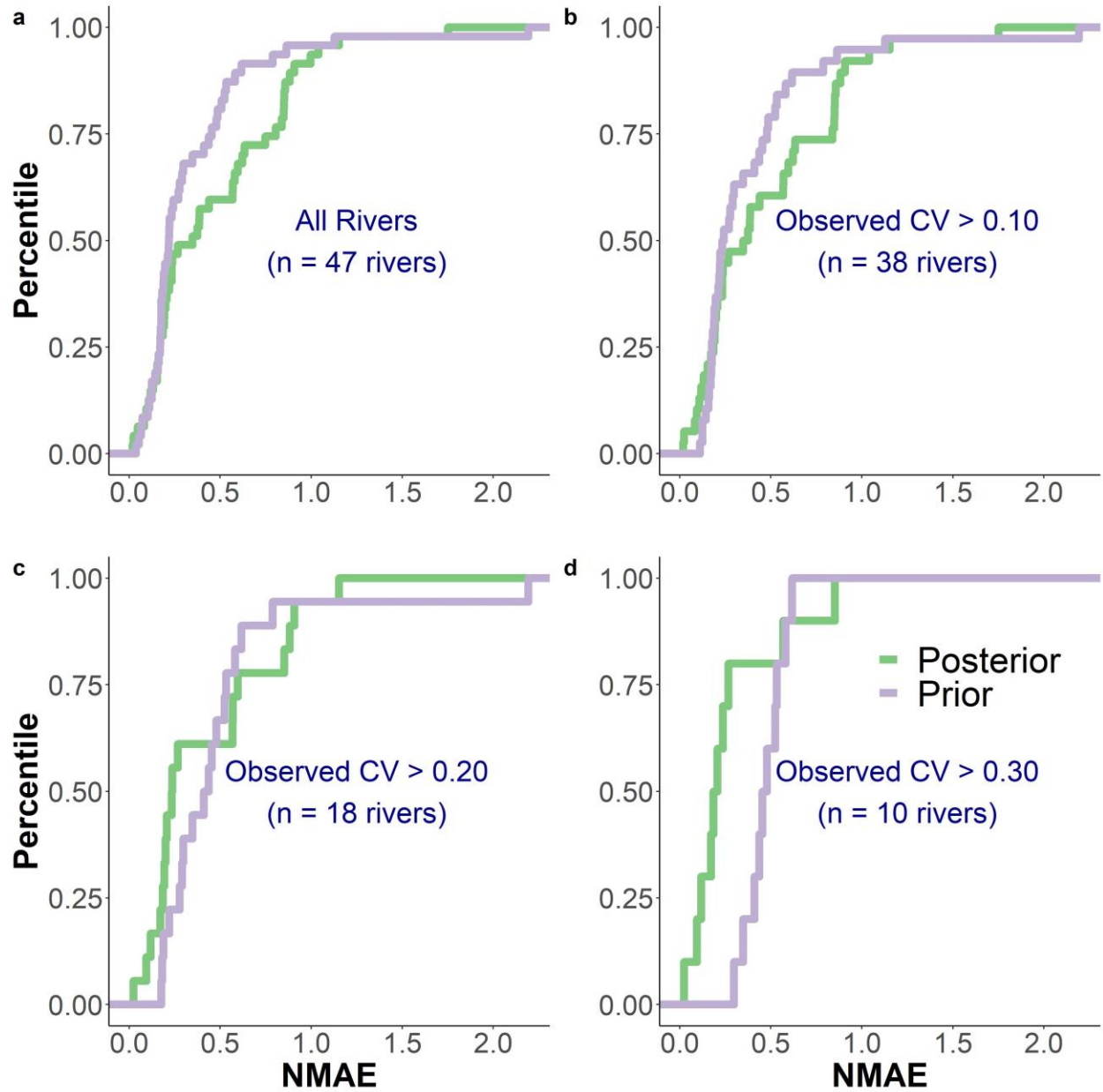475   We explore why this happens below.

Figure 6: Empirical cummulative density functions for prior and posterior k_{600} NMAE. See Table 1 for metric definition. a) all rivers. b) Only rivers with a coefficient of varaiton (CV) of observed k_{600} > 0.10. c) Only rivers with CV > 0.20. d) Only rivers with CV > 0.30. Overall we

480   *see that rivers with greater temporal variation in k_{600} behave better for BIKER, i.e. Bayesian*

481   *inference reduces bias from prior to posterior.*

482   Recall that BIKER relies on a timeseries of SWOT data, and that these timeseries may not

483   be representative of the full spectrum of k_{600} values that are actually experienced in the river,

484   therefore potentially biasing both the prior estimation methods (Text S3) and the actual Bayesian

485   inference. Put another way, we suggest that if a SWOT timeseries does not sufficiently capture a

486   river's temporal dynamics, it will introduce additional error to the inference results. To test this,

487   we subset our validation dataset by progressively higher coefficients of variation (*CV*) (> 10%,

488   >20%, and >30%). These filtered datasets are plotted in Figures 6b-6d (for > 10%, >20%, and

489   >30% *CV*, respectively), where our hypothesis is confirmed. Posterior bias drops once the temporal

490   variability of the SWOT data is sufficiently high, with BIKER posterior error the smallest, and

491   much less than prior error, in Figure 6d. This result is elaborated on in Section 4.2.

492   **3.3.2 Carbon Emissions**

493   Finally, we carry these FCO_2 calculations all the way to annual carbon emissions rates and

494   compare BIKER against established in situ techniques. It is important to remember that only

495   BIKER is completely globally implementable, while the other three models necessarily rely on

496   having a streamflow record or high-quality routed streamflow readily available. Therefore, the in

497   situ methods reflect their 'best-case scenarios' while BIKER reflects its worst case scenario, where

498   priors are set entirely from SWOT observations and are generally the least informative they will

499   ever be. This means that BIKER's annual carbon emission estimate can only improve from what

500   is presented here. We also stress again that the raw emissions rates here are largely meaningless

501   as they are calculated from an identical $CO_{2_{water}}$ timeseries applied to every river. We are

502   principally interested in relative differences between techniques employed.

503   Figure 7 compares the annual carbon emissions rate (via F_{CO_2}) from the rivers using BIKER

504   posterior means and the three stream gauge-based HG models. Surprisingly, BIKER outperforms

505   the gauge-based approaches, nearly correctly inferring the annual carbon emissions rate (9.8 Tg-

506   C/yr for BIKER versus 9.35 Tg-C/yr observed). The three HG models overestimate this emissions

507   rate: 14.8, 11.71, and 15.28 for 'Raymond 2013', 'Raymond 2012', and 'Brinkerhoff 2019'

508   respectively. 'Raymond 2012' falls within the BIKER CIs and is reasonably close to the observed

509   value, while 'Raymond 2013' overestimates the emission rate. 'Brinkerhoff 2019''s lower CI is

510   comparable to BIKER's higher CI. BIKER's relatively stronger performance than the in situ

511   models is elaborated on in Section 4.3. Finally, BIKER's uncertainity is on par with the in situ

512   technique ('Brinkerhoff 2019'), despite being obtained solely from SWOT data. Taken in

513   aggregate, BIKER provides a strong upscaling estimate of the annual carbon emission rate for the

514   rivers and is either comparable or better than established in situ techniques (Figure 7).
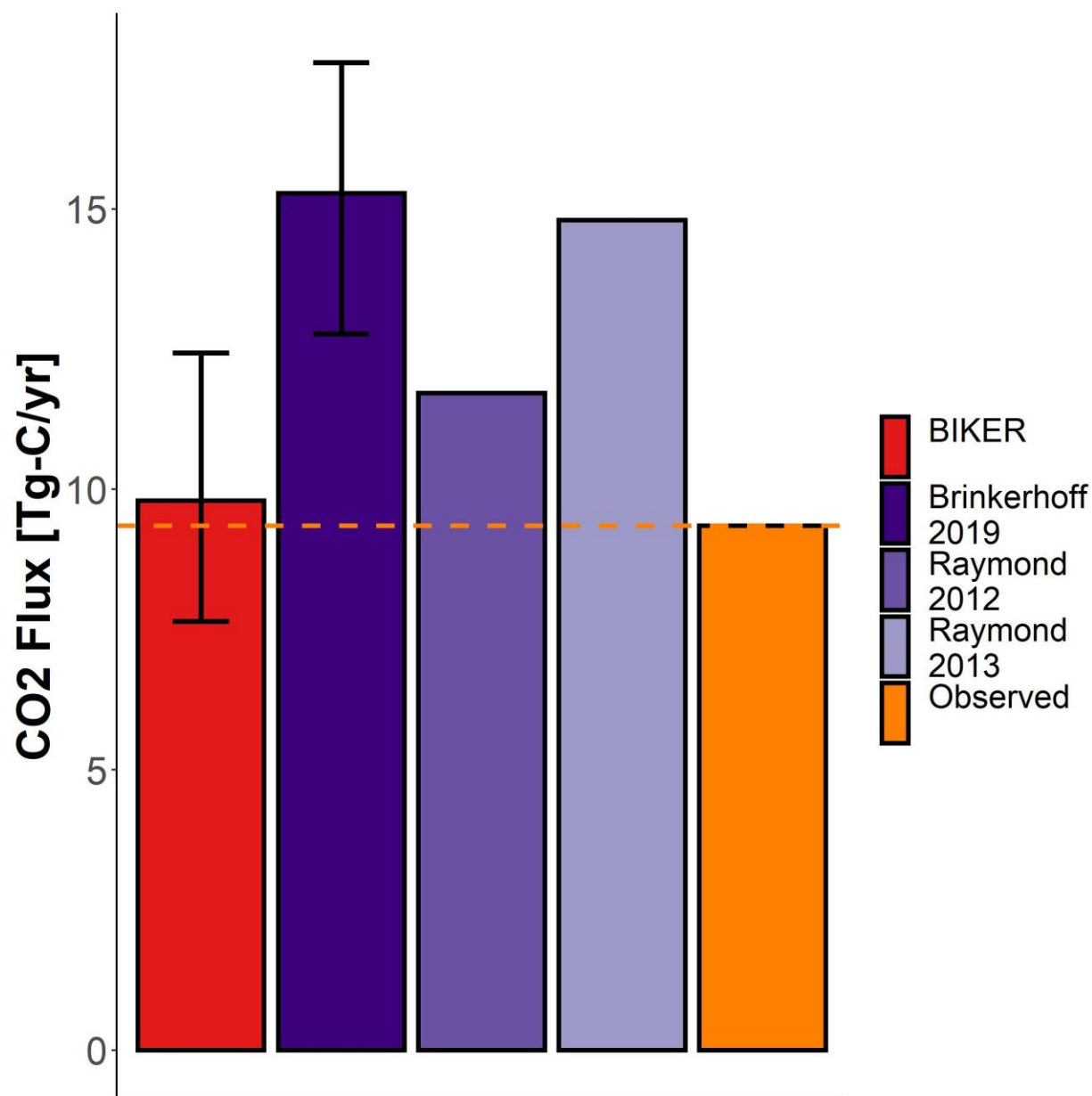
515

Figure 7: Yearly carbon emissions rate via CO_2 evasion across all rivers. Completely remotely-sensed methods are colored in red, in situ methods in purple, and the observed in orange. Note that confidence intervals were not calculated for the remaining two models because their uncertainties are not available.

520 **4 Discussion**

521   **4.1 Gas exchange in hydraulically-wide rivers**

522   Field studies of gas exchange in wide rivers have suggested that k_{600} behaves differently

523 in these rivers than in steeper and smaller rivers (Alin et al., 2011; Beaulieu et al., 2012; Raymond

524 & Cole, 2001; Ulseth et al., 2019; Wang et al., 2021). While much work has focused on the small-

525 stream side of the stream-to-river continuum, comparatively less work has been done in large

526 systems. Here, we focus on the larger, 'smooth-channel' end of the continuum, using a model for

527 gas exchange that scales k_{600} by both ϵ_D and a shear Reynold's number. This model is empirically

528 validated in Figure 2. Specifically, Figure S1 confirms that scaling k_{600} with a shear Reynold's

529 adaption of the small-eddy model (Equation 7) improves the model's predictions of the smallest

530 k_{600} values (where the relative decrease in turbulence reaching the surface is greater than the

531 small-eddy model alone suggests, per Equation 7's theoretical basis- Moog & Jirka, 1999a).

532 Scaling k_{600} via a shear Reynold's number is often done to parameterize breaking-wave gas

533 exchange models in the open ocean (Brumer et al., 2017; Zhao et al., 2003; Zhao & Toba, 2001),

534 though this is specific to high wind speeds in open ocean. To our knowledge, Moog & Jirka

535 (1999a)'s specific setup, which imposes a space-and-time varying, fractional area surface

536 turbulence theory on the small-eddy model, has never been empirically validated in rivers. Figure

537 2 provides this empirical verification for hydraulically wide channels, where it's theoretical basis

538 should generally hold. Using our full dataset of k_{600}, we also observed this model breaks down

539 when including non-hydraulically-wide rivers (as the theory would suggest). Future tests should

540 also explore other shear Reynold's scaling relations for gas exchange in rivers.

541   Crucially, we are not accounting for wind-driven gas exchange, which is suggested to play

542   an important role in wide rivers because river surface area is sufficiently large that sheltering no

543   longer limits the influence of wind-derived turbulence (Beaulieu et al., 2012; Raymond & Cole,

544   2001; Wang et al., 2021). None of the existing hydraulics-driven fluvial k_{600} models account for

545   wind-driven gas exchange either. Additionally, under higher-wind scenarios the turbulent regime

546   will switch from hydraulically-driven to wind-driven turbulence (Zappa et al., 2007) and the

547   assumptions under-pinning BIKER will likely break down. BIKER's outputs can therefore be

548   interpreted as the 'k_{600} under low-wind conditions', when surface turbulence is dominated by

549   hydraulics rather than wind. That said, BIKER's flexible implementation is a good start towards

550   eventually coupling hydraulics-driven gas exchange with wind-driven gas exchange under these

551   moderate-to-high wind scenarios. This is left to future work.

552   **4.2 Towards remote sensing of global spatiotemporal dynamics of k_{600} in large rivers**

553   To date, the studies exploring the spatiotemporal dynamics of riverine gas exchange have

554   arguably been held back by a lack of data. A few studies have investigated these dynamics, but

555   they have been limited to individual rivers and/or limited field seasons (Hall et al., 2012; Sand-

556   Jensen & Staehr, 2012). For example, Wallin et al. (2011) performed a preliminary analysis in

557   northern Sweden relating cross-section specific temporal variability in gas exchange with channel

558   slope, but they were limited to a mean of only 8 measurements per river in a single watershed.

559   While this is a good start, this is insufficient for further developing process-level understandings

560   of gas exchange at the global-scale.

561 Therefore, inferring k_{600} from SWOT data is an attractive option to address this problem

562 of limited data. For reference, 95% of the SWOT-visible rivers globally (202,811) will have

563 sufficient SWOT observations along the river to run BIKER at least once every 21 days, with most

564 of the temperate and Arctic rivers having 3+ observations per 21-day cycle (Altenau et al., 2021).

565 While BIKER will not directly measure k_{600}, it does robustly infer temporal trends in k_{600} and

566 reasonably infers the absolute magnitude of k_{600} (Figures 4-6). This much data will provide a

567 novel dataset of k_{600} on a scale never before possible.

568 With that said, Figures 4, 5, S4, and S5 all highlight a substantial range of BIKER

569 performance across rivers. These differences in performance are likely due to the

570 representativeness of the priors used for that river. This makes sense as Section 2 has effectively

571 reduced k_{600} to a function of hydraulics that are nearly all directly measurable by SWOT. Any

572 resulting bias in BIKER's predictions is likely attributable to either bias in the priors used for the

573 non-remotely sensed terms (Equations 9-10) or in the k_{600} model itself (Equation 7, including the

574 aforementioned wind errors). For SWOT discharge algorithms, authors have repeatedly shown

575 that the 'quality' of prior river knowledge plays a large role in the success of discharge inversions

576 (Andreadis et al., 2020; Brinkerhoff et al., 2020; Frasson et al., 2021; Tuozzolo et al., 2019) and

577 our results here further corroborate this finding.

578 Furthermore, Figure 6 implies that a sufficient variability in SWOT observations is

579 necessary to strongly infer a k_{600} timeseries. 'Hydraulic visibility', i.e. the ability of a remote

580 sensor to identify a hydrological response in the river (P.-A. Garambois et al., 2017) is applicable

581 here. If we apply hydraulic visibility to a sensor's ability to identify temporal variations in k_{600},

582 Figure 6 suggests that a 'minimally sufficient' hydraulic variability in SWOT measurements (in

583 Figure 6b, suggested to be approximately >20% *CV*) is needed to improve upon the prior. This

584 will be important once SWOT launches and BIKER is implemented at the global-scale.

585 **4.3 Coupling BIKER with upscaling workflows**

586 Figure 7 confirms that BIKER is quite successful at predicting annual upscaled carbon

587 emissions from the river network when coupled with CO_2 data. This encouraging result has three

588 main implications for future work.

589 First, Figure 7 directly implies that BIKER will be useful when coupled with large-scale

590 $CO_{2_{water}}$ models, provided these models are accurate. The models would give time and space

591 varying gas exchange. Liu et al. (2022) and Saccardi & Winnick (2021) each propose models that

592 robustly predict reach-scale dissolved CO_2 concentrations using two different approaches-

593 machine learning for Liu et al. (2022) and process-based reactive transport modeling for Saccardi

594 & Winnick (2021)- but both models yield CO_2 estimates that would be spatially and temporally

595 consistent with BIKER's output. Our promising results suggest that BIKER could provide

596 additional (and directly inferred) measurements of k_{CO_2} to these models, thereby better informing

597 model results through direct observations. This is likely to be accomplished via data assimilation

598 which has proven useful in using remotly-sensed discharge to improve streamflow routing models

599 (Feng et al., 2021; Ishitsuka et al., 2020), and of which the Saccardi & Winnick (2021) CO_2 model

600 takes a similar form.

601   Second, at the field-scale Figure 7 confirms that we can couple BIKER with in situ gas

602   concentration loggers to produce FCO_2 estimates at novel temporal resolutions in SWOT-

603   observable rivers. High temporal fidelity datasets of dissolved CO_2 in SWOT-observable rivers

604   now exist (e.g. Aho, Hosen, et al., 2021) but no such similar datasets for k_{CO_2} at equivalent

605   temporal resolutions exist. For rivers unobservable by SWOT, we further suggest that BIKER

606   could be run at the field scale (rather than via satellite-based altimeters like SWOT) using arrays

607   of in situ pressure transducers to estimate water surface slope following recent similar work for

608   estimating streamflow (Harlan et al., 2021). Regardless, both approaches would produce $CO_{2_{water}}$

609   and k_{CO_2} datasets at equivalent temporal resolution and allow us to directly calculate daily to sub-

610   daily CO_2 fluxes from river reaches.

611   Finally, Figure 7 also uniquely allows us to directly compare the influence of geomorphic

612   assumptions on total carbon emission rates from river networks, as all other calculations and

613   parameters were held constant across our four tested models (Text S5). Therefore, Figure 7

614   highlights a potentially large source of uncertainty in current river CO_2 upscaling estimates: the

615   geomorphic models employed to scale river channel hydraulics with streamflow. In this case, the

616   only difference between the three literature models and the observed estimate in Figure 7 is the

617   specific HG model employed to predict river depth and velocity (Text S5, Table S2), and yet the

618   eventual carbon emissions estimates (Figure 7) are quite different. Further, recall that the BIKER

619   results in Figure 7 reflect a worst-case scenario (relatively uniformed priors), while the three in-

620   situ methods represent best case scenarios (perfect streamflow records). We suggest future work

621   should perform a formal sensitivity analysis for these HG parameters.

622 **5 Conclusions**

623   The CO_2 flux from the global river network is a major natural component of the global

624 carbon cycle, on par with total forest carbon uptake (Pan et al., 2011). Despite much interest and

625 progress, there is still large uncertainty in the temporal dynamics of gas exchange and thus carbon

626 emissions to the atmosphere. Much of this uncertainty stems from uncertainty in k_{600} at the global

627 scale. In this paper, we propose that the soon-to-launch SWOT satellite will provide enough

628 hydraulic measurements to analyse the temporal dynamics of k_{600}, and therefore allow for a

629 global-scale analysis of spatiotemporal trends in large-river k_{600} once SWOT launches. In that

630 context, we developed 1) a hydraulic model for k_{600} that is nearly entirely SWOT observable and

631 explains 70% of variation in k_{600}, and 2) the BIKER algorithm to infer k_{600} using no on-the-

632 ground information. Validating on 47 SWOT-simulated rivers, we show strong recovery of rivers'

633 temporal k_{600} dynamics and a hypothetical total annual carbon emission rate across all 47 rivers.

634 These results suggest BIKER can be used to infer global-scale, near daily estimates of fluvial gas

635 exchange velocity once SWOT launches in late 2022. This in turn will be useful in mapping the

636 global-scale spatiotemporal dynamics of fluvial gas exchange in large rivers.

637 **6 Acknowledgements**

643 **7 Data availability statement**

644   Datasets required for this research are available from Ulseth et al. (2019)

645 (https://doi.org/10.1038/s41561-019-0324-8), Brinkerhoff et al. (2019)

646 (https://doi.org/10.1029/2019GL084529), Frasson et al. (2021)

647 (https://zenodo.org/record/3817817), Churchill et al. (1964)

648 (https://pubs.usgs.gov/pp/0737/report.pdf), Owens et al. (1964)

649 (https://pubs.usgs.gov/pp/0737/report.pdf), Beaulieu et al. (2012)

650 (https://doi.org/10.1029/2011JG001794), and Durand et al. (2016)

651 (https://doi.org/10.1002/2015WR018434). All code to build and generate results and figures is

652 archived at https://zenodo.org/record/6416069.

653 **8 Software availability statement**

654   The BIKER algorithm remains in active development and is available at

655 https://github.com/craigbrinkerhoff/BIKER. The specific version of BIKER used in this study is

656 archived at https://zenodo.org/record/6415434.

657 **9 Apendix A**

658   *Table A1: Variable description and notation for this study*

Notation	Description	Calculation (if not directly measured)	Units
A	Channel cross-sectional area		$[L^2]$
A_0	Non-SWOT-observable cross-sectional area		$[L^2]$

Notation	Description	Calculation (if not directly measured)	Units
A_p	Active zone fraction (Moog & Jirka 1999)	$A_p \propto Re_*^{1/2}$ (Moog & Jirka 1999)	$dimensionless$
α	Statistical parameter for Equation S5 scaling relation		$\dfrac{m^{1/2}s^{3/4}}{dy}$
α_1	Statistical parameter for Equation S7 scaling relation		$\dfrac{m^{1/2}s^{3/4}}{dy}$
β	Statistical parameter for Equation S13 scaling relation		$\dfrac{m^{-1/4}s^{9/8}}{dy}$
β_1	Statistical parameter for Equation 7 scaling relation		$\dfrac{m^{1/2}s^{3/4}}{dy}$
$CO_{2_{water}}$	Water-side CO_2 concentration		$\left[\dfrac{M}{L^3}\right]$
$CO_{2_{air}}$	Atmospheric-side CO_2 concentration		$\left[\dfrac{M}{L^3}\right]$
dA	change in cross-sectional area	$\delta H_e * W$	$[L]$
D_m	Molecular diffusion coefficient		$\left[\dfrac{L^2}{T}\right]$
ϵ	Dissipation rate of near-surface turbulence		$\left[\dfrac{E}{M*T}\right]$
ϵ_S	log-law-of-the-wall model for ϵ	$\dfrac{U_*^3}{H}$	$\left[\dfrac{E}{M*T}\right]$
ϵ_D	Form-drag model for ϵ	$gS\bar{U}$	$\left[\dfrac{E}{M*T}\right]$
FCO_2	CO_2 evasion flux from river to atmosphere		$\left[\dfrac{M}{L^2T}\right]$
$FCO_{2_{upscaled}}$	Upscaling estimate of the global CO_2 evasion flux from river to atmosphere		$\left[\dfrac{M}{L^2T}\right]$
g	gravitational acceleration	9.8	$\left[\dfrac{L}{T^2}\right]$
H	Mean flow depth	$\dfrac{A}{W}$	$[L]$
H_e	Water surface elevation		$[L]$

Notation	Description	Calculation (if not directly measured)	Units
i	Cross-section discretization within a mass-conserved river reach		
k	gas exchange velocity		$\left[\dfrac{L}{T}\right]$
k_{600}	gas exchange velocity normalized to $Sc = 600$	$\left(\dfrac{600}{Sc}\right)^{-0.5} k$	$\left[\dfrac{L}{T}\right]$
n	Manning's roughness coefficient	$\dfrac{R_h^{2/3} S^{1/2}}{\bar{U}}$	$\left[\dfrac{T}{L^3}\right]$
ρ	Density of water		$\left[\dfrac{M}{L^{1/3}}\right]$
Q	River discharge	$WH\bar{U}$	$\dfrac{L^3}{T}$
R_h	Hydraulic radius	$\dfrac{AW}{2H+W}$	$[L]$
Re_8	Shear Reynold's numbers	$\dfrac{U_* H}{v}$	dimensionless
S	River slope		dimensionless
Sc	Schmidt number	$\dfrac{v}{D_m}$	
t	timestep discretization within river reach		
Θ	Bayesian parameter set		
$\bar{U}$	Cross-sectional average velocity	$\dfrac{Q}{A}$	$\left[\dfrac{L}{T}\right]$
U_*	Shear velocity	$\sqrt{gSR_h}$	$\left[\dfrac{L}{T}\right]$
μ	Viscosity		$[P*T]$
v	kinematic viscosity	$\dfrac{\mu}{\rho}$	$\left[\dfrac{L^2}{T}\right]$
W	Flow width		$[L]$
x	Bayesian data set		

659 **References**

660   Aho, K. S., & Raymond, P. A. (2019). Differential Response of Greenhouse Gas Evasion

661 to Storms in Forested and Wetland Streams. *Journal of Geophysical Research: Biogeosciences*,

662 *124*(3), 649–662. https://doi.org/10.1029/2018JG004750

663   Aho, K. S., Fair, J. H., Hosen, J. D., Kyzivat, E. D., Logozzo, L. A., Rocher-Ros, G., et al.

664 (2021). Distinct concentration-discharge dynamics in temperate streams and rivers: CO2 exhibits

665 chemostasis while CH4 exhibits source limitation due to temperature control. *Limnology and*

666 *Oceanography*, *66*(10), 3656–3668. https://doi.org/10.1002/lno.11906

667   Aho, K. S., Hosen, J. D., Logozzo, L. A., McGillis, W. R., & Raymond, P. A. (2021).

668 Highest rates of gross primary productivity maintained despite CO2 depletion in a temperate river

669 network.   *Limnology   and   Oceanography   Letters*,   *n/a*(n/a).

670 https://doi.org/https://doi.org/10.1002/lol2.10195

671   Alin, S. R., Rasera, M. de F. F. L., Salimon, C. I., Richey, J. E., Holtgrieve, G. W., Krusche,

672 A. V., & Snidvongs, A. (2011). Physical controls on carbon dioxide transfer velocity and flux in

673 low-gradient river systems and implications for regional carbon budgets. *Journal of Geophysical*

674 *Research: Biogeosciences*, *116*(G1). https://doi.org/https://doi.org/10.1029/2010JG001398

675   Altenau, E. H., Pavelsky, T. M., Durand, M. T., Yang, X., Frasson, R. P. de M., & Bendezu,

676 L. (2021). The Surface Water and Ocean Topography (SWOT) Mission River Database

677 (SWORD): A Global River Network for Satellite Data Products. *Water Resources Research*, *57*(7),

678 e2021WR030054. https://doi.org/10.1029/2021WR030054

679   Andreadis, K. M., Brinkerhoff, C. B., & Gleason, C. J. (2020). Constraining the

680   assimilation of SWOT observations with hydraulic geometry relations. *Water Resources Research*.

681   https://doi.org/10.1029/2019WR026611

682   Appling, A. P., Hall, R. O., Yackulic, C. B., & Arroita, M. (2018). Overcoming

683   Equifinality: Leveraging Long Time Series for Stream Metabolism Estimation. *Journal of*

684   *Geophysical   Research: Biogeosciences*,   *123*(2),   624–645.

685   https://doi.org/https://doi.org/10.1002/2017JG004140

686   Beaulieu, J. J., Shuster, W. D., & Rebholz, J. A. (2012). Controls on gas transfer velocities

687   in   a   large   river.   *Journal   of   Geophysical   Research: Biogeosciences*,   *117*(G2).

688   https://doi.org/10.1029/2011JG001794

689   Biancamaria, S., Lettenmaier, D. P., & Pavelsky, T. M. (2016). The SWOT Mission and

690   Its Capabilities for Land Hydrology. In A. Cazenave, N. Champollion, J. Benveniste, & J. Chen

691   (Eds.), *Remote Sensing and Water Resources* (pp. 117–147). Cham: Springer International

692   Publishing. https://doi.org/10.1007/978-3-319-32449-4_6

693   Borges, A. V., Darchambeau, F., Teodoru, C. R., Marwick, T. R., Tamooh, F., Geeraert,

694   N., et al. (2015). Globally significant greenhouse-gas emissions from African inland waters.

695   *Nature Geoscience*, *8*(8), 637–642. https://doi.org/10.1038/ngeo2486

696   Brinkerhoff, C. B., Gleason, C. J., & Ostendorf, D. W. (2019). Reconciling at-a-Station

697   and at-Many-Stations Hydraulic Geometry Through River-Wide Geomorphology. *Geophysical*

698   *Research Letters*, *46*(16), 9637–9647. https://doi.org/10.1029/2019GL084529

699   Brinkerhoff, C. B., Gleason, C. J., Feng, D., & Lin, P. (2020). Constraining Remote River

700   Discharge Estimation Using Reach-Scale Geomorphology. *Water Resources Research*, *56*(11),

701   e2020WR027949. https://doi.org/https://doi.org/10.1029/2020WR027949

702   Brinkerhoff, C. B., Raymond, P. A., Maavara, T., Ishitsuka, Y., Aho, K. S., & Gleason, C.

703   J. (2021). Lake Morphometry and River Network Controls on Evasion of Terrestrially Sourced

704   Headwater CO2. *Geophysical Research Letters*, *48*(1), e2020GL090068.

705   https://doi.org/https://doi.org/10.1029/2020GL090068

706   Brisset, P., Monnier, J., Garambois, P.-A., & Roux, H. (2018). On the assimilation of

707   altimetric data in 1D Saint–Venant river flow models. *Advances in Water Resources*, *119*, 41–59.

708   https://doi.org/10.1016/j.advwatres.2018.06.004

709   Brumer, S. E., Zappa, C. J., Blomquist, B. W., Fairall, C. W., Cifuentes-Lorenzen, A.,

710   Edson, J. B., et al. (2017). Wave-Related Reynolds Number Parameterizations of CO2 and DMS

711   Transfer Velocities. *Geophysical Research Letters*, *44*(19), 9865–9875.

712   https://doi.org/10.1002/2017GL074979

713   Calderbank, P. H., & Moo-Young, M. B. (1961). The continuous phase heat and mass-

714   transfer properties of dispersions. *Chemical Engineering Science*, *16*(1), 39–54.

715   https://doi.org/10.1016/0009-2509(61)87005-X

716   Churchill, M. A., Elmore, H. L., & Buckingham, R. A. (1964). The Prediction of Stream

717   Reaeration Rates. In B. A. Southgate (Ed.), *Advances in Water Pollution Research* (pp. 89–136).

718   Pergamon. https://doi.org/10.1016/B978-1-4832-8391-3.50015-4

46

719   Cole, J. J., Prairie, Y. T., Caraco, N. F., McDowell, W. H., Tranvik, L. J., Striegl, R. G., et

720   al. (2007). Plumbing the Global Carbon Cycle: Integrating Inland Waters into the Terrestrial

721   Carbon Budget. *Ecosystems*, *10*(1), 172–185. https://doi.org/10.1007/s10021-006-9013-8

722   Crawford, J. T., Stanley, E. H., Dornblaser, M. M., & Striegl, R. G. (2017). CO2 time series

723   patterns in contrasting headwater streams of North America. *Aquatic Sciences*, *79*(3), 473–486.

724   https://doi.org/10.1007/s00027-016-0511-2

725   Durand, M. T., Neal, J., Rodríguez, E., Andreadis, K. M., Smith, L. C., & Yoon, Y. (2014).

726   Estimating reach-averaged discharge for the River Severn from measurements of river water

727   surface elevation and slope. *Journal of Hydrology*, *511*, 92–104.

728   https://doi.org/10.1016/j.jhydrol.2013.12.050

729   Durand, M. T., Gleason, C. J., Garambois, P. A., Bjerklie, D., Smith, L. C., Roux, H., et

730   al. (2016). An intercomparison of remote sensing river discharge estimation algorithms from

731   measurements of river height, width, and slope. *Water Resources Research*, *52*(6), 4527–4549.

732   https://doi.org/10.1002/2015WR018434

733   Durand, M. T., Chen, C., Moraes Frasson, R. P. de, Pavelsky, T. M., Williams, B., Yang,

734   X., & Fore, A. (2020). How will radar layover impact SWOT measurements of water surface

735   elevation and slope, and estimates of river discharge? *Remote Sensing of Environment*, *247*,

736   111883. https://doi.org/10.1016/j.rse.2020.111883

737   Feng, D., Gleason, C. J., Lin, P., Yang, X., Pan, M., & Ishitsuka, Y. (2021). Recent changes

738 to Arctic river discharge. *Nature Communications*, *12*(1), 6917. https://doi.org/10.1038/s41467-

739 021-27228-1

740   Frasson, R. P. de M., Durand, M. T., Larnier, K., Gleason, C., Andreadis, K. M.,

741 Hagemann, M., et al. (2021). Exploring the factors controlling the error characteristics of the

742 Surface Water and Ocean Topography mission discharge estimates. *Water Resources Research*,

743 *n/a*(n/a), e2020WR028519. https://doi.org/https://doi.org/10.1029/2020WR028519

744   Garambois, P.-A., & Monnier, J. (2015). Inference of effective river properties from

745 remotely sensed observations of water surface. *Advances in Water Resources*, *79*, 103–120.

746 https://doi.org/10.1016/j.advwatres.2015.02.007

747   Garambois, P.-A., Calmant, S., Roux, H., Paris, A., Monnier, J., Finaud-Guyot, P., et al.

748 (2017). Hydraulic visibility: Using satellite altimetry to parameterize a hydraulic model of an

749 ungauged reach of a braided river. *Hydrological Processes*, *31*(4), 756–767.

750 https://doi.org/10.1002/hyp.11033

751   Garambois, P.-A., Larnier, K., Monnier, J., Finaud-Guyot, P., Verley, J., Montazem, A.-

752 S., & Calmant, S. (2020). Variational estimation of effective channel and ungauged anabranching

753 river discharge from multi-satellite water heights of different spatial sparsity. *Journal of*

754 *Hydrology*, *581*, 124409. https://doi.org/10.1016/j.jhydrol.2019.124409

755   Gleason, C. J. (2015). Hydraulic geometry of natural rivers: A review and future directions.

756   *Progress in Physical Geography: Earth and Environment*, *39*(3), 337–360.

757   https://doi.org/10.1177/0309133314567584

758   Gleason, C. J., & Smith, L. C. (2014). Toward global mapping of river discharge using

759   satellite images and at-many-stations hydraulic geometry. *Proceedings of the National Academy*

760   *of Sciences*, *111*(13), 4788–4791. https://doi.org/10.1073/pnas.1317606111

761   Gleason, C. J., Smith, L. C., & Lee, J. (2014). Retrieval of river discharge solely from

762   satellite imagery and at-many-stations hydraulic geometry: Sensitivity to river form and

763   optimization parameters. *Water Resources Research*, *50*(12), 9604–9619.

764   https://doi.org/10.1002/2014WR016109

765   Gleason, C. J., Garambois, P.-A., & Durand, M. T. (2017). Tracking River Flows from

766   Space. *Eos*. https://doi.org/10.1029/2017EO078085

767   Gruber, N., Clement, D., Carter, B. R., Feely, R. A., Heuven, S. van, Hoppema, M., et al.

768   (2019). The oceanic sink for anthropogenic CO_2 from 1994 to 2007. *Science*, *363*(6432), 1193–

769   1199. https://doi.org/10.1126/science.aau5153

770   Hagemann, M. W., Gleason, C. J., & Durand, M. T. (2017). BAM: Bayesian AMHG-

771   Manning Inference of Discharge Using Remotely Sensed Stream Width, Slope, and Height. *Water*

772   *Resources Research*, *53*(11), 9692–9707. https://doi.org/10.1002/2017WR021626

773   Hall, R. O., & Ulseth, A. J. (2020). Gas exchange in streams and rivers. *WIREs Water*,

774   *7*(1), e1391. https://doi.org/https://doi.org/10.1002/wat2.1391

775   Hall, R. O., Kennedy, T. A., & Rosi-Marshall, E. J. (2012). Air–water oxygen exchange in

776   a large whitewater river. *Limnology and Oceanography: Fluids and Environments*, *2*(1), 1–11.

777   https://doi.org/https://doi.org/10.1215/21573689-1572535

778   Harlan, M. E., Gleason, C. J., Altenau, E. H., Butman, D., Carter, T., Chu, V. W., et al.

779   (2021). Discharge Estimation from Dense Arrays of Pressure Transducers. *Water Resources*

780   *Research*, *n/a*(n/a), e2020WR028714. https://doi.org/https://doi.org/10.1029/2020WR028714

781   Hoff, P. D. (2009). *A First Course in Bayesian Statistical Methods*. New York: Springer.

782   Horgby, Å., Segatto, P. L., Bertuzzo, E., Lauerwald, R., Lehner, B., Ulseth, A. J., et al.

783   (2019). Unexpected large evasion fluxes of carbon dioxide from turbulent streams draining the

784   world's mountains. *Nature Communications*, *10*(1). https://doi.org/10.1038/s41467-019-12905-z

785   Ishitsuka, Y., Gleason, C. J., Hagemann, M. W., Beighley, E., Allen, G. H., Feng, D., et al.

786   (2020). Combining optical remote sensing, McFLI discharge estimation, global hydrologic

787   modelling, and data assimilation to improve daily discharge estimates across an entire large

788   watershed.   *Water   Resources   Research*,   *n/a*(n/a).

789   https://doi.org/https://doi.org/10.1029/2020WR027794

790   Katul, G., Mammarella, I., Grönholm, T., & Vesala, T. (2018). A Structure Function Model

791   Recovers the Many Formulations for Air-Water Gas Transfer Velocity. *Water Resources*

792   *Research*, *54*(9), 5905–5920. https://doi.org/https://doi.org/10.1029/2018WR022731

793   Knoben, W. J. M., Freer, J. E., & Woods, R. A. (2019). Technical note: Inherent benchmark

794   or not? Comparing Nash–Sutcliffe and Kling–Gupta efficiency scores. *Hydrology and Earth*

795   *System Sciences*, *23*(10), 4323–4331. https://doi.org/10.5194/hess-23-4323-2019

796   Lamont, J. C., & Scott, D. S. (1970). An Eddy Cell Model of Mass Transfer into the Surface

797   of a Turbulent Liquid. *AIChE Journal*, *16*(4), 513–519.

798   Larnier, K., Monnier, J., Garambois, P.-A., & Verley, J. (2020). River discharge and

799   bathymetry estimation from SWOT altimetry measurements. *Inverse Problems in Science and*

800   *Engineering*, *0*(0), 1–31. https://doi.org/10.1080/17415977.2020.1803858

801   Lauerwald, R., Laruelle, G. G., Hartmann, J., Ciais, P., & Regnier, P. A. G. (2015). Spatial

802   patterns in CO2 evasion from the global river network. *Global Biogeochemical Cycles*, *29*(5), 534–

803   554. https://doi.org/10.1002/2014GB004941

804   Leopold, L. B., & Maddock, T. (1953). *The Hydraulic Geometry of Stream Channels and*

805   *Some Physiographic Implications*. U.S. Government Printing Office.

806   Liu, S., & Raymond, P. A. (2018). Hydrologic controls on pCO2 and CO2 efflux in US

807   streams   and   rivers.   *Limnology   and   Oceanography   Letters*,   *3*(6),   428–435.

808   https://doi.org/10.1002/lol2.10095

809   Liu, S., Kuhn, C., Amatulli, G., Aho, K., Butman, D. E., Allen, G. H., et al. (2022). The

810   importance of hydrology in routing terrestrial carbon to the atmosphere via global streams and

811   rivers.   *Proceedings   of   the   National   Academy   of   Sciences*,   *119*(11),   e2106322119.

812   https://doi.org/10.1073/pnas.2106322119

813   Lorke, A., & Peeters, F. (2006). Toward a Unified Scaling Relation for Interfacial Fluxes.

814   *Journal of Physical Oceanography*, *36*(5), 955–961. https://doi.org/10.1175/JPO2903.1

815   Moog, D. B., & Jirka, G. H. (1999a). Air-Water Gas Transfer in Uniform Channel Flow.

816   *Journal of Hydraulic Engineering*, *125*(1), 3–10. https://doi.org/10.1061/(ASCE)0733-

817   9429(1999)125:1(3)

818   Moog, D. B., & Jirka, G. H. (1999b). Stream Reaeration in Nonuniform Flow:

819   Macroroughness Enhancement. *Journal of Hydraulic Engineering*, *125*(1), 6.

820   Oubanas, H., Gejadze, I., Malaterre, P.-O., Durand, M., Wei, R., Frasson, R. P. M., &

821   Domeneghetti, A. (2018). Discharge Estimation in Ungauged Basins Through Variational Data

822   Assimilation: The Potential of the SWOT Mission. *Water Resources Research*, *54*(3), 2405–2423.

823   https://doi.org/10.1002/2017WR021735

824   Owens, M., Edwards, R. W., & Gibbs, J. W. (1964). Some reaeration studies in streams.

825   *Inter. J. Air Water Poll.*, *8*, 469–486. Retrieved from https://ci.nii.ac.jp/naid/10025707421/

826   Pan, Y., Birdsey, R. A., Fang, J., Houghton, R., Kauppi, P. E., Kurz, W. A., et al. (2011).

827   A Large and Persistent Carbon Sink in the World's Forests. *Science*, *333*(6045), 988–993.

828   https://doi.org/10.1126/science.1201609

829   Peter, H., Singer, G. A., Preiler, C., Chifflard, P., Steniczka, G., & Battin, T. J. (2014).

830   Scales and drivers of temporal pCO2 dynamics in an Alpine stream. *Journal of Geophysical*

831   *Research: Biogeosciences*,   *119*(6),   1078–1091.

832   https://doi.org/https://doi.org/10.1002/2013JG002552

833   Ran, L., Lu, X. X., & Liu, S. (2017). Dynamics of riverine CO2 in the Yangtze River fluvial

834 network and their implications for carbon evasion. *Biogeosciences*, *14*, 2183–2198.

835   Raymond, P. A., & Cole, J. J. (2001). Gas Exchange in Rivers and Estuaries: Choosing a

836 Gas Transfer Velocity. *Estuaries*, *24*(2), 312–317. https://doi.org/10.2307/1352954

837   Raymond, P. A., Bauer, J. E., & Cole, J. J. (2000). Atmospheric CO2 evasion, dissolved

838 inorganic carbon production, and net heterotrophy in the York River estuary. *Limnology and*

839 *Oceanography*, *45*(8), 1707–1717. https://doi.org/https://doi.org/10.4319/lo.2000.45.8.1707

840   Raymond, P. A., Zappa, C. J., Butman, D., Bott, T. L., Potter, J., Mulholland, P., et al.

841 (2012). Scaling the gas transfer velocity and hydraulic geometry in streams and small rivers.

842 *Limnology and Oceanography*, 41–53. https://doi.org/10.1215/21573689-

843 1597669@10.1002/(ISSN)1939-5590.MethaneVI

844   Raymond, P. A., Hartmann, J., Lauerwald, R., Sobek, S., McDonald, C., Hoover, M., et al.

845 (2013). Global carbon dioxide emissions from inland waters. *Nature*, *503*(7476), 355–359.

846 https://doi.org/10.1038/nature12760

847   Rocher-Ros, G., Sponseller, R. A., Lidberg, W., Mörth, C.-M., & Giesler, R. (2019).

848 Landscape process domains drive patterns of CO2 evasion from river networks. *Limnology and*

849 *Oceanography Letters*, *4*(4), 87–95. https://doi.org/10.1002/lol2.10108

850   Saccardi, B., & Winnick, M. (2021). Improving Predictions of Stream CO2 Concentrations

851 and Fluxes Using a Stream Network Model: A Case Study in the East River Watershed, CO, USA.

852 *Global Biogeochemical Cycles*, *35*(12), e2021GB006972. https://doi.org/10.1029/2021GB006972

853   Sand-Jensen, K., & Staehr, P. A. (2012). CO2 dynamics along Danish lowland streams:

854   Water–air gradients, piston velocities and evasion rates. *Biogeochemistry*, *111*(1), 615–628.

855   https://doi.org/10.1007/s10533-011-9696-6

856   Talke, S. A., Horner-Devine, A. R., Chickadel, C. C., & Jessup, A. T. (2013). Turbulent

857   kinetic energy and coherent structures in a tidal river. *Journal of Geophysical Research: Oceans*,

858   *118*(12), 6965–6981. https://doi.org/10.1002/2012JC008103

859   Tokoro, T., Kayanne, H., Watanabe, A., Nadaoka, K., Tamura, H., Nozaki, K., et al.

860   (2008). High gas-transfer velocity in coastal regions with high energy-dissipation rates. *Journal of*

861   *Geophysical Research: Oceans*, *113*(C11). https://doi.org/10.1029/2007JC004528

862   Tuozzolo, S., Lind, G., Overstreet, B., Mangano, J., Fonstad, M., Hagemann, M., et al.

863   (2019). Estimating River Discharge With Swath Altimetry: A Proof of Concept Using AirSWOT

864   Observations.   *Geophysical   Research   Letters*,   *46*(3),   1459–1466.

865   https://doi.org/10.1029/2018GL080771

866   Ulseth, A. J., Hall, R. O., Boix Canadell, M., Madinger, H. L., Niayifar, A., & Battin, T. J.

867   (2019). Distinct air–water gas exchange regimes in low- and high-energy streams. *Nature*

868   *Geoscience*, *12*(4), 259–263. https://doi.org/10.1038/s41561-019-0324-8

869   Vachon, D., Prairie, Y. T., & Cole, J. J. (2010). The relationship between near-surface

870   turbulence and gas transfer velocity in freshwater systems and its implications for floating chamber

871   measurements   of   gas   exchange.   *Limnology   and   Oceanography*,   *55*(4),   1723–1732.

872   https://doi.org/10.4319/lo.2010.55.4.1723

873   Wallin, M. B., Öquist, M. G., Buffam, I., Billett, M. F., Nisell, J., & Bishop, K. H. (2011).

874   Spatiotemporal variability of the gas transfer coefficient (KCO2) in boreal streams: Implications

875   for large scale estimates of CO2 evasion. *Global Biogeochemical Cycles*, *25*(3).

876   https://doi.org/https://doi.org/10.1029/2010GB003975

877   Wang, J., Bombardelli, F. A., & Dong, X. (2021). Physically Based Scaling Models to

878   Predict Gas Transfer Velocity in Streams and Rivers. *Water Resources Research*, *57*(3),

879   e2020WR028757. https://doi.org/https://doi.org/10.1029/2020WR028757

880   Zappa, C. J., Raymond, P. A., Terray, E. A., & McGillis, W. R. (2003). Variation in surface

881   turbulence and the gas transfer velocity over a tidal cycle in a macro-tidal estuary. *Estuaries*, *26*(6),

882   1401–1415. https://doi.org/10.1007/BF02803649

883   Zappa, C. J., McGillis, W. R., Raymond, P. A., Edson, J. B., Hintsa, E. J., Zemmelink, H.

884   J., et al. (2007). Environmental turbulent mixing controls on air-water gas exchange in marine and

885   aquatic systems. *Geophysical Research Letters*, *34*(10). https://doi.org/10.1029/2006GL028790

886   Zhao, D., & Toba, Y. (2001). Dependence of Whitecap Coverage on Wind and Wind-Wave

887   Properties. *Journal of Oceanography*, *57*(5), 603–616. https://doi.org/10.1023/A:1021215904955

888   Zhao, D., Toba, Y., Suzuki, Y., & Komori, S. (2003). Effect of wind waves on air'sea gas

889   exchange: Proposal of an overall CO2 transfer velocity formula as a function of breaking-wave

890   parameter. *Tellus B: Chemical and Physical Meteorology*, *55*(2), 478–487.

891   https://doi.org/10.3402/tellusb.v55i2.16747